NLTE 1.5D Modelling of Red Giant Stars

by

Mitchell Young

A Thesis Submitted to
Saint Mary's University, Halifax, Nova Scotia
in Partial Fulfillment of the Requirements for
the Degree of Master of Science in Astronomy
(Department of Astronomy and Physics)

August 21^{st}, 2013, Halifax, Nova Scotia

Approved: Dr. Ian Short (Supervisor)

Approved: Dr. Robert Deupree (Examiner)

Approved: Dr. Philip Bennett (Examiner)

Date: August 21^{st}, 2013.

Acknowledgments

I would like to first thank my supervisor, Dr. Ian Short, for giving me this opportunity, for his insight, advice, and guidance, and most of all, for his considerable patience with me. Without him believing in me, I never could have made it all the way here. Thank you as well to Dr. Robert Deupree and Dr. Philip Bennett for being on my defense committee and taking the time to read this work, and to the Faculty of Graduate Studies and Research for helping to fund this work.

Next I would like to thank all of my colleagues, Anneya, Bobby, Chris, Dan, Dave, Diego, James, Jason, Liz, Michael, and Mike for all of their advice and support, and most of all Chris, Kirsten, Patrick, and Sherry for going through this ordeal with me.

"*All you really need to know for the moment is that the universe is a lot more complicated that you might think, even if you start from a position of thinking it's pretty damn complicated in the first place.*"

–Douglas Adams

This thesis is dedicated to Albert Walzak, my grandfather, who did not get to see me finish, but was the first man to show me the stars.

Contents

List of Figures

List of Tables

Abstract

NLTE 1.5D Modelling of Red Giant Stars

by Mitchell Young

Spectra for 2D stars in the 1.5D approximation are created from synthetic spectra of 1D non-local thermodynamic equilibrium (NLTE) model atmospheres produced by the PHOENIX code. The 1.5D stars assume the spatially averaged modelling parameters of a standard K3-4 III star, while varying the temperature difference between the two components ($\Delta T_{1.5\mathrm{D}}$). Synthetic observable quantities from the 1.5D stars are fitted with quantities from 1D models to assess the errors in inferred T_{eff} values from assuming horizontal homogeneity and local thermodynamic equilibrium (LTE). Five different quantities are fit to determine the T_{eff} of the 1.5D stars. In all cases except the TiO bands, the T_{eff} value increases with increasing $\Delta T_{1.5\mathrm{D}}$, up to 500 K greater than the average of the 1.5D star. In all cases, the inferred T_{eff} value from fitting 1D LTE quantities is between 25 K and 150 K higher than from fitting 1D NLTE quantities. This differential modelling study should permit constraints on the extent of T_{eff} inhomogeneities in red giants by comparing 1.5D models with observations.

August 21^{st}, 2013

Chapter 1

Introduction

1.1 Red Giant Stars

Red giant stars rank among the brightest stars in the Galaxy. Located in the upper right portion of the Hertzsprung-Russell (H-R) diagram in the red giant branch (RGB), as seen in Fig. 1.1, they are generally much brighter in the visible band than main sequence stars of the same spectral type, but this only partially accounts for their brightness as large portion of their flux is emitted in the near-IR. Because of their enormous surface area, this gives them high luminosity such that they are easily observable even in very remote stellar populations. This grants us a tool for probing nearly all regions of the Galaxy using a common indicator, a feat unparalleled by most other types of stars.

Because red giants are low to intermediate mass stars that have evolved beyond the main sequence, generally found in older stellar populations, their abundances are indicators of early Galactic chemical evolution. For example, by comparing observations of Galactic bulge giants with those of giants located in the thin and thick disks and halo, it has been shown that the bulge likely experienced similar formation timescales, chemical evolution histories, star formation rates and initial mass functions as the local thick disk population (Meléndez et al. 2008; Alves-Brito et al.

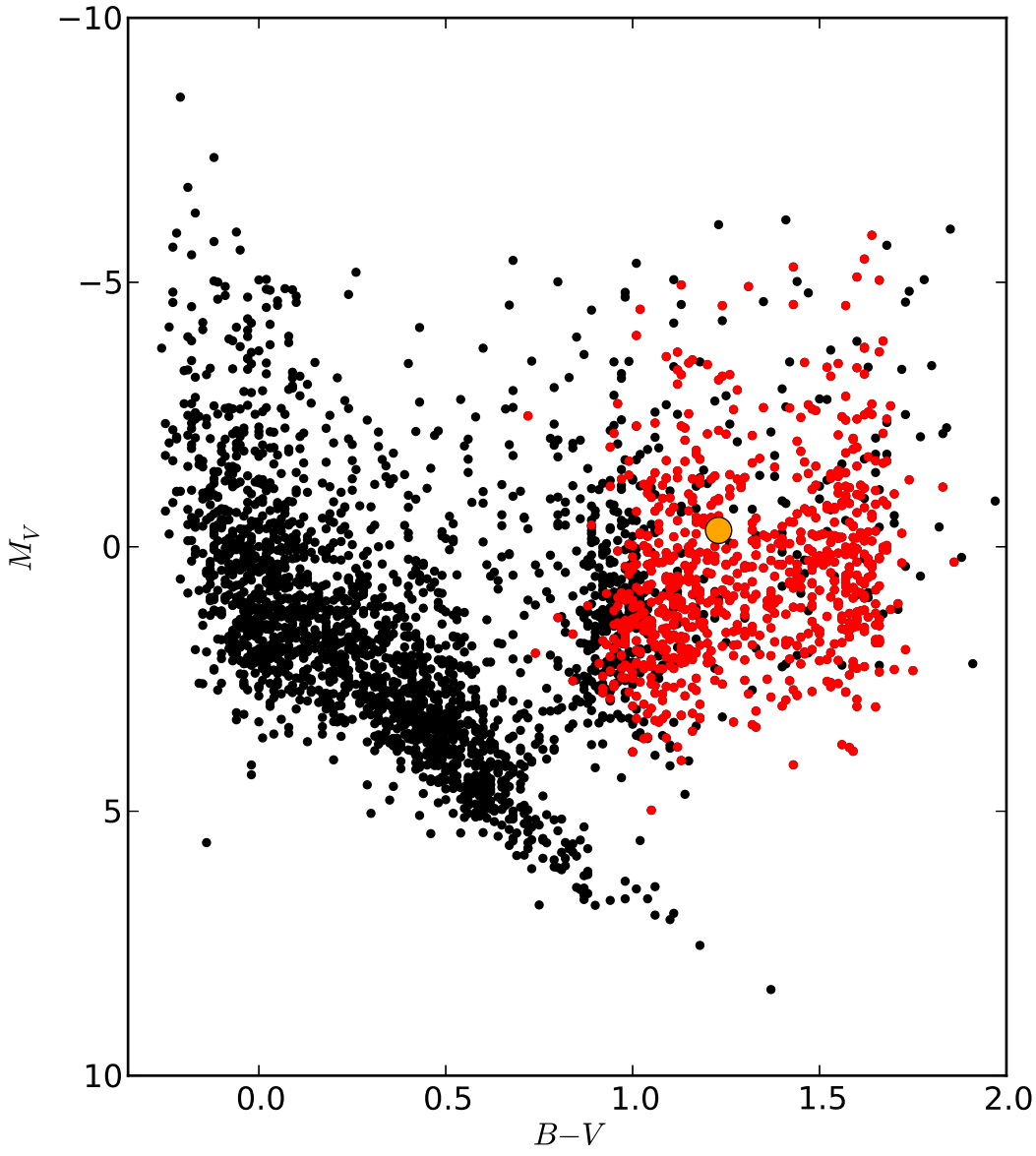

Figure 1.1: Observer's H-R diagram of 3182 stars in the Yale Bright Star Catalogue 5th edition (Hoffleit & Jaschek 1991) with recorded values for visual magnitude V, B-V colour index, and trigonometric parallax. Giant stars of MK spectral class K or M are marked in red. The large orange marker denotes Arcturus, a typical early K giant star.

2010). Bulge and disk giants show some differences in their chemical abundances, with the bulge giants showing a higher relative abundance of select elements than the disk giants, suggesting more rapid chemical enrichment, possibly by ejecta from supernovae of Types Ia and II (Cunha & Smith 2006). Observations of red clump giants in the bulge have also produced additional evidence of a central bar in the bulge (Stanek et al. 1997), with their apparent visual magnitudes being brighter at some Galactic latitudes than others.

The tip of the RGB (TRGB) is also used as a standard candle to determine distances to nearby galaxies. The distance moduli obtained from the I pass-band magnitude of the TRGB are comparable with those from primary distance indicators like Cepheids and RR Lyraes (Makarov et al. 2006), and in some cases even suggest a reevaluation of the metallicity dependence and zero point calibration of the Cepheid distance scale (Salaris & Cassisi 1998; Rizzi et al. 2007). The TRGB method even has advantages over other distance determinations like those of Cepheids and RR Lyraes: (1) the TRGB method requires much less telescope time than variable stars; (2) the I magnitude of the TRGB is insensitive to the variation of metallicity for $[\mathrm{Fe/H}] < -0.7$; and (3) the TRGB suffers less from extinction problems than Cepheids, which are in general located in star-forming regions (Lee et al. 1993).

1.2 Modelling Stellar Atmospheres

A stellar atmosphere is the outer region of a star, surrounding the interior, and acts as a transition region from the stellar interior to the interstellar medium. This region represents somewhere between a fraction of a percent and a few percent of the total stellar radius (R_0), inversely proportional to the surface gravity (g) of the star. For observational purposes, the atmosphere is the most important region of a star, because the atmosphere is where the visible stellar spectrum originates.

Stellar atmospheres are modelled to compute observable quantities, such as spectral energy distributions (SEDs), spectral line profiles, or photometric colours, based upon the current theory of stellar atmospheric structure. While these quantities are all fundamentally connected, and many of

the refinements in modelling techniques apply to all of them, these quantities are independently used for comparison with observed quantities to determine stellar parameters and elemental abundances in stars. In turn, these can give information on a star's local environment and neighbours, or place constraints on the age of the star and at what epoch it was formed.

Much of what is now known about all types of stars comes from fitting the predicted quantities from atmospheric models to observations. Estimates of the solar chemical abundances come from fitting synthetic spectral line profiles and equivalent widths to those observed in the Sun (Ross & Aller 1976; Asplund et al. 2009; Caffau et al. 2011). Calibrations of stellar parameters, such as g, absolute visual magnitude, $T_{\rm eff}$, luminosity, and R_0, for different spectral types are found from fitting models (Martins et al. 2005). Beyond studying single stars, model atmospheres can be used to determine qualities of larger structures as well. The age-metallicity and colour-metallicity relations of globular clusters can be determined from the abundances of individual red giants within the clusters (Pilachowski et al. 1983; Carretta & Gratton 1997; Carretta et al. 2010).

Because a stellar atmosphere is a complex environment, some or all of a number of simplifying approximations may be used when modelling them. In cases cases where the geometric extent of the atmosphere is much smaller than the radius of the star, plane-parallel geometry can be assumed, otherwise spherical geometry is adopted, as here.

Horizontal homogeneity assumes that all position dependent modelling variables, such as temperature or density, vary only along the vertical depth axis and are constant over a surface of given depth. Models that adopt horizontal homogeneity and either plane-parallel or spherical geometry are considered to be one dimensional (1D) models because calculations only have one independent variable, the depth coordinate.

Assuming time-independence for the atmosphere prevents the number densities of ionization stages and atomic and molecular energy levels, defined by the statistical equilibrium (SE) equations, at every point in the atmosphere from changing.

Hydrostatic equilibrium assumes that there is no net radial force acting on any point within the atmosphere, and that the outward pressure gradient is balanced by the gravitational force. This

assumption implies that the star is not variable, such as a pulsator, a star with a strong wind, or a nova.

In local thermodynamic equilibrium (LTE), all gas particle level populations, including atomic, ionic, and molecular populations, are given by Saha-Boltzmann statistics defined by the local value of the kinetic temperature ($T_{\rm Kin}$), and the radiative source function (S_λ) is given by $S_\lambda = B_\lambda(T = T_{\rm Kin})$, where B_λ is the Planck function. However, the radiation field intensity (I_λ) is allowed to depart from B_λ, otherwise strict thermodynamic equilibrium would hold, and there would be no temperature gradient, and no outward transfer of radiant energy.

1.3 Present Work

In this work, we will explore the limitations of two of the simplifying assumptions of atmospheric modelling: horizontal homogeneity and LTE. Both of these assumptions have been adopted because they are more computationally practical than the alternatives, requiring less time and fewer resources to arrive at a result. Horizontal inhomogeneity requires model atmospheres to be calculated in two or three geometric dimensions (2D or 3D models), and non-LTE (NLTE) requires that each level population be computed in SE using an iterative process.

However, horizontal homogeneity and LTE both limit how realistic a model can be. Simulations of red giant atmospheres performed in 3D have confirmed that turbulent surface convection causes horizontal inhomogeneities to form (Collet et al. 2007; Kučinskas et al. 2013a), such as visually observable surface features like solar granulation (Mathur et al. 2011; Tremblay et al. 2013). These features lead to detectable effects such as altering predicted line strengths and shapes and, thus, inferred elemental abundances (Collet et al. 2008, 2009; Hayek et al. 2011; Kučinskas et al. 2013b; Mashonkina et al. 2013). For 3D models of red giant atmospheres, whose modelling parameters span the ranges of 3600 K $\leq T_{\rm eff} \leq$ 5200 K, 1.0 $\leq \log g \leq$ 5.0, and -3.0 $\leq$ [Fe/H] $\leq$ 0.0, granules have been shown to span a range of sizes from as small as being on the order of 10^8 cm to as large as 2×10^{12} cm, with the majority being on the order of 10^{11} cm (Collet et al. 2007; Chiavassa et al.

2010; Hayek et al. 2011; Ludwig & Kučinskas 2012; Magic et al. 2013a; Tremblay et al. 2013). The cooler stars and stars with lower values of $\log g$ generally display larger features. For the same set of 3D models, the temperature among these features at optical depth unity varies by up to 2000 K between the hot and cool areas, centered around the $T_{\rm eff}$ of the model Collet et al. (2008, 2009); Kučinskas et al. (2013b,a); Magic et al. (2013b). Most of the 3D models reported in the literature have $T_{\rm eff} \approx 4500$ K, with ΔT varying by ~ 1000 K.

The most noticeable departure of LTE models from observed stars comes from comparing computed and observed spectral features and SEDs. In 1D and 3D models of red giants, NLTE models have been shown to be more accurate than LTE models in predicting the overall monochromatic flux (F_λ) levels of the SEDs and strength of individual spectral lines, with the notable exceptions of molecular absorption bands and the near-UV band flux (Short & Hauschildt 2003, 2006, 2009; Bergemann et al. 2013). Calculating the molecular level populations in NLTE is computationally demanding, and is not handled in many atmospheric modelling codes. Both LTE and NLTE models overpredict the near-UV F_λ levels of cool red giants. In the case of the near-UV F_λ levels, NLTE models are worse in the overprediction than their LTE counterparts. The NLTE effects of Fe group elements on the model structure and F_λ distribution have been shown to be much more important for predicting a SED than the NLTE effects of all the light metals combined, and serve to substantially increase the near-UV F_λ levels as a result of NLTE Fe I overionization (Short & Hauschildt 2009). This increase of the near-UV F_λ levels in NLTE is also shown, by Short & Hauschildt (2009), to be metallicity dependent, generally increasing with decreasing metallicity. These failures of 1D NLTE models to predict observable quantities may be, in part, related to the exclusion of horizontal inhomogeneities in the models. Therefore, this thesis aims to explore the relationship between NLTE and inhomogeneity on the predicted SED.

One of our primary goals is to isolate and quantify the errors that the horizontal homogeneity and LTE approximations introduce into $T_{\rm eff}$ values derived from observable quantities, such as photometric colours, SEDs, and rectified spectra, when fitting 1D LTE and NLTE models to spectra of horizontally inhomogeneous stars. The key idea for stars with horizontal inhomogeneities, where

the average $T_{\rm eff}$ of the variations is the same as the $T_{\rm eff}$ of a horizontally homogeneous star, is that the SED will depend on the variation of the modelling parameters across the surface. For example, using the Planck function,

$$B_\lambda(T_{\rm eff}) = \frac{2hc^2}{\lambda^5}\left(e^{\frac{hc}{\lambda k_B T_{\rm eff}}} - 1\right)^{-1}, \tag{1.1}$$

where h is Planck's constant, c is the speed of light, λ is the wavelength, and k_B is Boltzmann's constant, to describe the shape of a stellar continuum immediately illustrates an issue. For a star with a range of differing temperatures across the surface that covers over 1000 K, it is not directly obvious what value of $T_{\rm eff}$ should be used. Because of the non-linear dependence on $T_{\rm eff}$, this is an important question. The higher temperature material will contribute disproportionately more flux than the lower temperature material, with a dependence on wavelength, and will alter the spectrum from that of a horizontally homogeneous star of the same average $T_{\rm eff}$ accordingly.

We will also be investigating the relation between errors introduced in determining a star's $T_{\rm eff}$ from assuming horizontal homogeneity and those introduced by assuming LTE. The error inherent in assuming LTE is expected to remain approximately constant for different levels of horizontal inhomogeneity, as any changes in a LTE spectrum caused by the inhomogeneities should also be represented to a similar degree in the corresponding NLTE spectrum, as the relative difference in the flux distribution between LTE and NLTE should remain roughly constant within the $T_{\rm eff}$ range studied in this work.

Finally, we will compare our artificially inhomogeneous spectra with two sets of observed spectral data for Arcturus, a spectrophotometric SED and a high resolution spectral atlas, to present an example of how horizontal inhomogeneities present in the atmosphere of a red giant may be detected.

Chapter 2

Methods of Model Atmosphere Production and Analysis

In general, the calculation of a 2D model atmosphere requires a very substantial increase in computational effort over that needed for 1D models. However, there are two limiting cases for which the situation simplifies; these are often referred to as 1.5D models. One case is when the geometric scale of the inhomogeneities is small compared to the scale height (H) of the atmosphere, so that every emergent ray may be assumed to have fully sampled both components of the atmosphere many times. This effectively makes the atmosphere 1D on the scale of H, but with constituent properties (i.e. opacity, density, etc.) that depend upon both components. In this case, the resultant constituent properties could be approximated by a linear combination of the original 1D components. The other limiting case, which is that adopted for this work, occurs when the scale of the inhomogeneities is large compared to H ($\sim 3 \times 10^9$ cm, given the modelling parameters listed in Section 2.1). If it is further assumed that there are only two distinct components making up the horizontally inhomogeneous structure, then the emergent flux from each component forms independently of the other. In this case, assumed to be applicable to this study, the emergent 1.5D model flux becomes simply a linear combination of the individual 1D component fluxes, weighted by the horizontal filling factor of each 1D component. It is further assumed that the size

of the inhomogeneities remains small compared to the stellar radius. Then, spherical symmetry is maintained to a good approximation (provided the inhomogeneities are uniformly distributed across the stellar surface), and the necessity of computing the angle integrals of the emergent intensities is avoided. A linear combination of surface fluxes can be used instead. By assuming features of the average size of modelled red giant granules, the stars modelled in this work have on the order of $\sim$1000 granules spread across their surfaces, more than enough to produce an even distribution of hot and cool features.

Two-dimensional information such as the difference in temperature among features or the relative portion of the stellar surface covered by the different features can be approximated by choosing the parameters of the 1D components being averaged, and the averaging weights. These 1.5D representations, approximating 2D effects, are treated as artificial "observations" of real stars that are fitted with a library of 1D trial models for inferring the $T_{\rm eff}$ of the 1.5D stars. A grid of 50 1D stellar model atmospheres and corresponding synthetic spectra was produced for this purpose using the PHOENIX code, adopting the parameters of a canonical K3-4 III star as a test case.

2.1 PHOENIX

The PHOENIX code can be used to model atmospheres and spectra of stellar objects throughout the H-R diagram (Baron & Hauschildt 1998; Hauschildt et al. 1997; Brott & Hauschildt 2005). This work utilized PHOENIX version 15 for all modelling calculations. The code models stellar atmospheres in part by solving the radiative transfer equation in spherical geometry. By performing the calculations using spherical coordinates, and by assuming horizontal homogeneity for the atmospheres, PHOENIX produces 1D model atmospheric structures. For canonical K3-4 III stars, the geometric extent of the atmosphere represents $\sim$1-2 % of the total stellar radius, suggesting that the use of spherically symmetric models would be more appropriate than the plane-parallel approximation. The term 1D implies the assumption that all of the parameters vary positionally only along the depth axis. This assumption is valid in the case where the mean free photon path is

much less than the horizontal distances over which features in the atmosphere vary. In the case of stellar objects, this is generally a useful assumption because the variation in small scale observable solar features such as granules and intergranular lanes occur on a scale of the order 10^7 to 10^8 cm, and modelling suggests larger surface features, up to $\sim 10^{12}$ cm, are present in red giant stars (Ludwig & Kučinskas 2012). For the models studied in this thesis, the photonic mean free path was found to be $\sim 1.5 \times 10^9$ cm at $\tau_{5000} \approx 1$, much smaller than predicted granules in red giants.

Solving the radiative transfer equation requires PHOENIX to calculate the extinction caused by millions of spectral lines for both atomic and molecular species and some of their associated ionization stages. PHOENIX has two options for computing the population of the associated energy levels for each line. The code can either work in LTE, which is computationally simple by comparison, or the more realistic NLTE, treatment. Under the LTE assumption, radiation and matter are assumed to be in local equilibrium everywhere in the atmosphere. The $T_{\rm Kin}$ of the gas may then be substituted for the excitation, ionization, and radiation temperatures ($T_{\rm Exc}$, $T_{\rm Ion}$, and $T_{\rm Rad}$ respectively). This further allows the simplification of setting $S_\lambda = B_\lambda(T = T_{\rm Rad})$, with $T_{\rm Rad} = T_{\rm Kin}$, where $S_\lambda = j_\lambda / k_\lambda$, where j_λ and k_λ are the emission and absorption coefficients respectively. Energy levels are then populated using the Saha-Boltzmann distribution. While this is computationally simple compared to the NLTE treatment, it is less realistic. In the NLTE regime, the radiation and matter temperatures are no longer coupled, and PHOENIX uses an iterative procedure to solve the coupled radiative transfer and NLTE statistical equilibrium equations. To compute the level populations, PHOENIX includes tens of thousands of NLTE bound-bound (b-b) transitions with this method, for each of which the rate equation is solved individually. For the computational times to be small enough to be convenient, the code is capable of being operated on parallel processors. Only four CPUs were used in this work to ensure that no problems arose from inter-processor communications. It is important to include NLTE effects because they can lead to a difference in the blue and near-UV bands flux of up to 50% over corresponding LTE models of red giant stars as a result of NLTE Fe overionization (Short & Hauschildt 2003). This effect is displayed in Fig. 2.1.

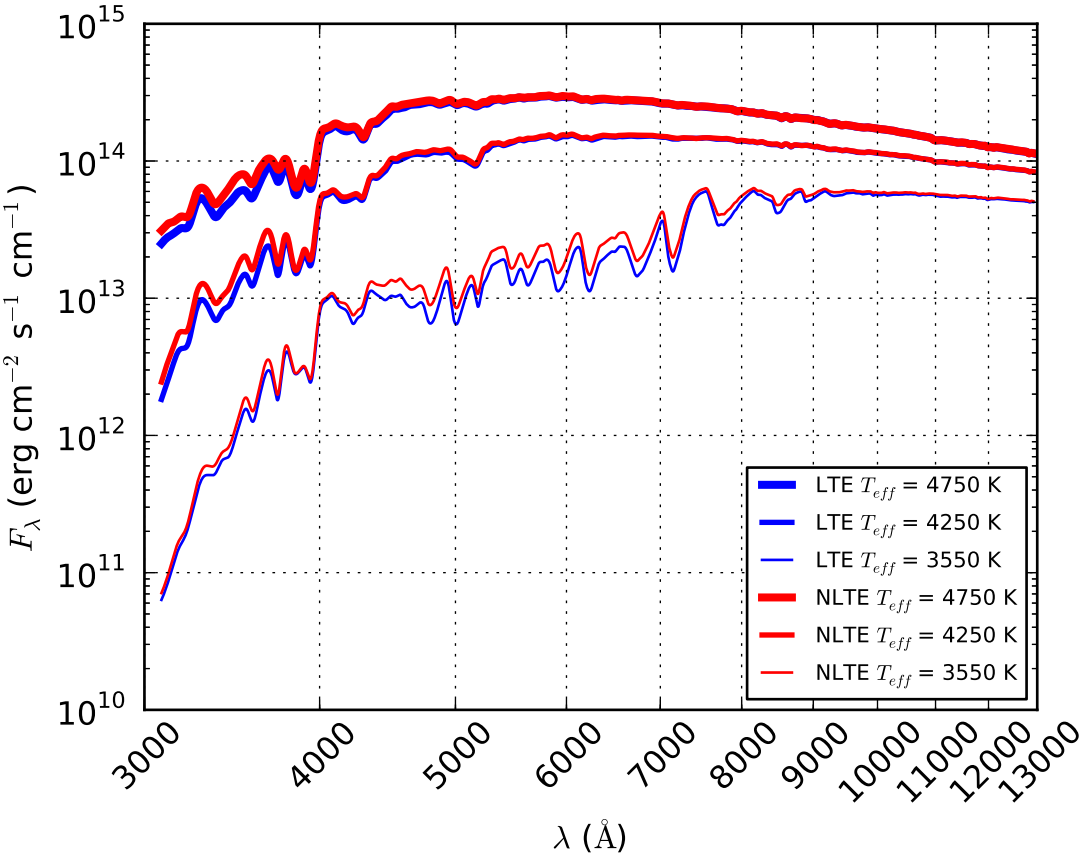

Figure 2.1: PHOENIX LTE and NLTE synthetic spectra generated from the hottest and coolest grid models and the canonical early K giant model. The high resolution spectra generated by PHOENIX were convolved with a FWHM = 50 Å Gaussian kernel, and the convolved spectra are displayed. The LTE spectra with $T_{\rm eff} = 4250$ K and 4750 K are mostly hidden behind their NLTE counterparts.

The stellar parameters adopted for a canonical K3-4 III star are $T_{\rm eff}$ = 4250 K, log g = 2.0, and [M/H] = -0.5 with the alpha elements, from O to Ti, enhanced by [A/H] = +0.3. The radius of the star is defined by $g = GM/R_0^2$, where G is the gravitational constant, and is set to $R_0 = 1.1512573 \times 10^{12}$ cm by adopting a value for the mass M to be M =1 $M_\odot$; the convective mixing length parameter, α, was set to α =1, and the microturbulent velocity parameter, ξ_T, was set to $\xi_T = 1.0$ km s^{-1}. The model atmospheres were all sampled at 64 discrete monochromatic optical depth (τ_λ) points ranging from $\tau_{1.2\,\mu{\rm m}}$ = 10^{-6} to 10^2, covering the atmosphere from a point where it is optically very thin at all wavelengths in the visible band to a point well after it becomes optically thick. The NLTE models were constructed by treating the 20 atomic species listed in Table 2.1 as NLTE species when calculating energy level populations, all of them in the neutral state and most in the singly ionized state as well (Short & Hauschildt 2005). With the exception of $T_{\rm eff}$, all of the listed modelling parameters were held constant throughout our grid.

NLTE radiative equilibrium is complex in that any given transition may either heat or cool the atmosphere with respect to LTE, depending on how rapidly τ_λ increases inward at the transition wavelength, whether the transition is located in the Wien or Rayleigh-Jeans regime, and whether the transition is a net heater or cooler in LTE with respect to the gray atmosphere (Short et al. 2012). For our $T_{\rm eff}$ range , all of the NLTE models exhibit a surface cooling effect in the outermost layers of the atmosphere. This is displayed in Fig. 2.2 as a lower temperature in the NLTE models than in the LTE ones for a given τ_{12000}. For the majority of the upper atmosphere, between $\tau_{12000} \approx 10^{-4}$ and 10^{-1}, the opposite is seen, with the NLTE models having a higher temperature than the LTE ones.

To prepare the grid of models, the $T_{\rm eff}$ value was varied from 3550 K to 4750 K, with $\Delta T_{\rm eff}$ =50 K, and we produced both LTE and NLTE models. All LTE atmospheric models were converged in 10 iterations from neighbouring models within 200 K starting from the canonical K giant LTE model. Where possible, NLTE models were converged in 15 iterations from their LTE counterparts, with the exception of the $T_{\rm eff}$ = 4450 K model that failed to converge from the LTE 4450 K model, and was instead converged from the NLTE 4550 K model. While PHOENIX does not

Table 2.1: List of atomic species treated in NLTE energy level calculations. Number of energy levels and line transitions included for each ionization stage are given.

Element	I	II
H	80/3160	-
He	19/37	-
Li	57/333	55/124
C	228/1387	-
N	252/2313	-
O	36/66	-
Ne	26/37	-
Na	53/142	35/171
Mg	273/835	72/340
Al	111/250	188/1674
Si	329/1871	93/436
P	229/903	89/760
S	146/349	84/444
K	73/210	22/66
Ca	194/1029	87/455
Ti	395/5279	204/2399
Mn	316/3096	546/7767
Fe	494/6903	617/13675
Co	316/4428	255/2725
Ni	153/1690	429/7445

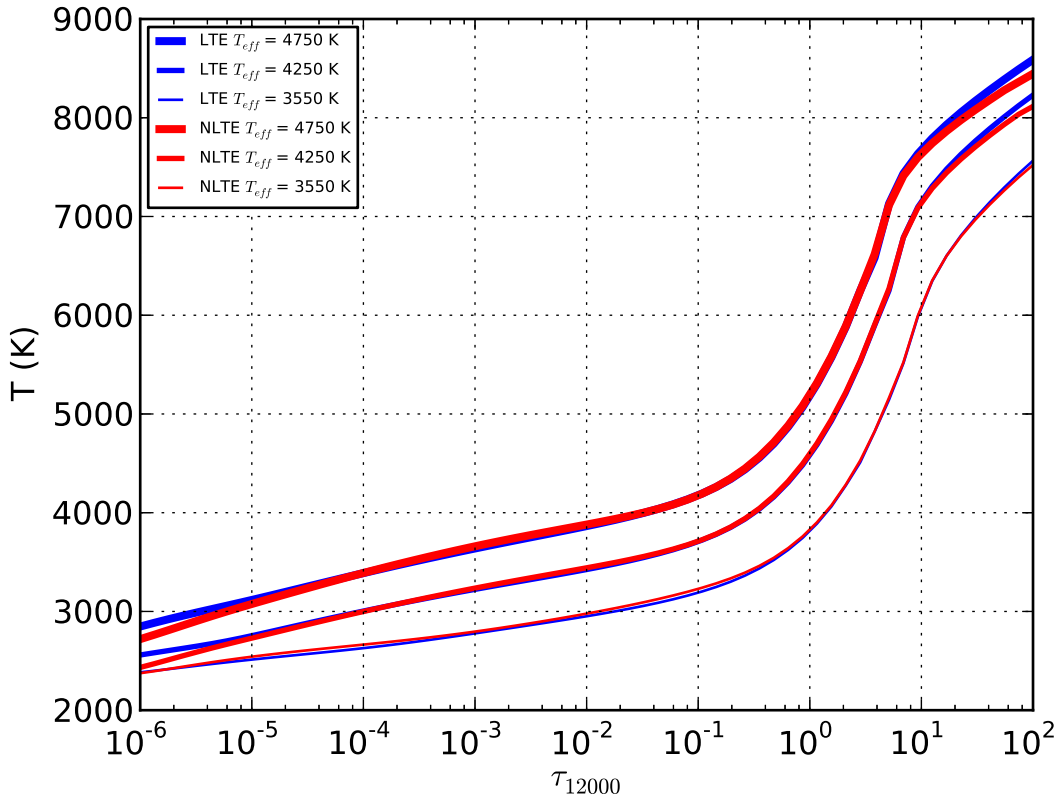

Figure 2.2: $T(\tau)$ relationships for PHOENIX LTE and NLTE atmospheric models representing the hottest and coolest grid models, along with the canonical models.

Table 2.2: Wavelength grid spacing used in computing PHOENIX model atmospheres and spectra

Wavelength Range λ (Å)	Spacing $\Delta\lambda$ (Å)	Mid Range Spectral Resolution R
3000-4000	0.010	350000
4000-5000	0.013	346000
5000-6000	0.016	344000
6000-7000	0.020	325000
7000-8000	0.023	326000
8000-11000	0.027	352000
11000-13000	0.037	324000

internally test for convergence, it does record the percent deviation of the bolometric flux from exact thermal equilibrium for each depth point at each iteration. Models were considered to have converged successfully if, after the final iteration, all of these values above the convective zone in the atmosphere were less than 1.0 %. Within the convective zone, energy is primarily transported by convective currents and not radiation, so the value of the percent deviation is meaningless.

Upon convergence of a model structure, two different spectra were synthesized for each model, the fully line blanketed SED and the pure continuum SED for use in normalizing the flux in the line blanketed SEDs. In synthesizing the continuum SEDs, PHOENIX ignores all atomic and molecular lines, and only includes continuum extinction sources such as photoionization. This calculation is always performed in LTE even when synthesizing the continuum of a NLTE model because PHOENIX cannot omit the NLTE b-b transitions in the calculations when synthesizing a spectrum. In all spectral synthesis cases, the SEDs are sampled from $\lambda = 3000$ Å to 13000 Å as shown in Table 2.2, with variable spacings, $\Delta\lambda$, to approximately preserve the spectral resolution, $R = \lambda/\Delta\lambda$, across the full range at $R \approx 300000$ to 400000. In the Wien regime the spacing is the smallest at $\Delta\lambda$ = 0.01 Å, and in the Rayleigh-Jeans tail the spacing is the largest at $\Delta\lambda$ = 0.037 Å. In addition to this, the NLTE SEDs are sampled at supplementary points that ensure each NLTE spectral line is critically sampled; these points are automatically distributed over each line by PHOENIX.

In addition to these synthetic spectra, another special type of SED was synthesized for the select LTE models $T_{\rm eff}$ = 3550 K, 4250 K, and 4750 K, representing the coolest and hottest models in the grid, and the standard reference canonical K giant model, by utilizing the PHOENIX Line ID

mode. This mode provides as output, for each wavelength sampling point, the depth index of both the continuum and total extinction optical depth points closest to unity as well as the identity of the strongest atomic contributor to the extinction coefficient at the sample point, and the strongest molecular contributor as well, if available.

Finally, to increase the apparent formal numerical resolution of the grid's $T_{\rm eff}$ range sampling, additional SEDs were linearly interpolated between neighbouring SEDs in the grid to reach a final apparent temperature resolution of 25 K. This was done to smooth the final fitted $T_{\rm eff}$ versus degree of inhomogeneity relation. However, we note that this does not decrease the formal uncertainty of the $T_{\rm eff}$ determination. Straight linear interpolation of the flux values was used instead of interpolating the log flux values because at the small ratio of $\Delta T_{\rm eff}/T_{\rm eff}$, the relative difference of the monochromatic flux ($\Delta F_\lambda/F_\lambda$) between the two methods was less than 1.0 % at all wavelength sampling points. Fig. 2.3 shows an example of the the difference in averaging methods when averaging the LTE SEDs with $T_{\rm eff}$ = 4700 K and 4750 K.

2.2 1.5D SED generation, post-processing, and analysis

Seventeen unique 1.5D SEDs representing 2D effects were each produced from two synthetic NLTE 1D SEDs while enforcing that the linear average of their $T_{\rm eff}$ values be 4250 K. This value of average $T_{\rm eff}$ was chosen to maintain a consistent observational property among all of the 1.5D SEDs. At long wavelengths far enough out in the Rayleigh-Jeans tail of a stellar spectrum, the continuum flux will have a linear dependence on $T_{\rm eff}$. This dependence is used by Infrared Flux Method (Ramírez & Meléndez 2005) to determine $T_{\rm eff}$, called the $RJ\,T_{\rm eff}$ in this work, from observations of the Rayleigh-Jeans tail of the stellar spectrum. Because of the linear dependence on $T_{\rm eff}$ in the Rayleigh-Jeans limit, the production of 1.5D SEDs by linear averaging of the component fluxes results in SEDs with identical Rayleigh-Jeans tails, and identical $RJ\,T_{\rm eff}$ values of 4250 K.

Two different methods were used in creating the 1.5D SEDs: 1) Selecting the 1D components such that the difference between their respective $T_{\rm eff}$ values ($\Delta T_{\rm 1.5D}$) was a multiple of 100 K,

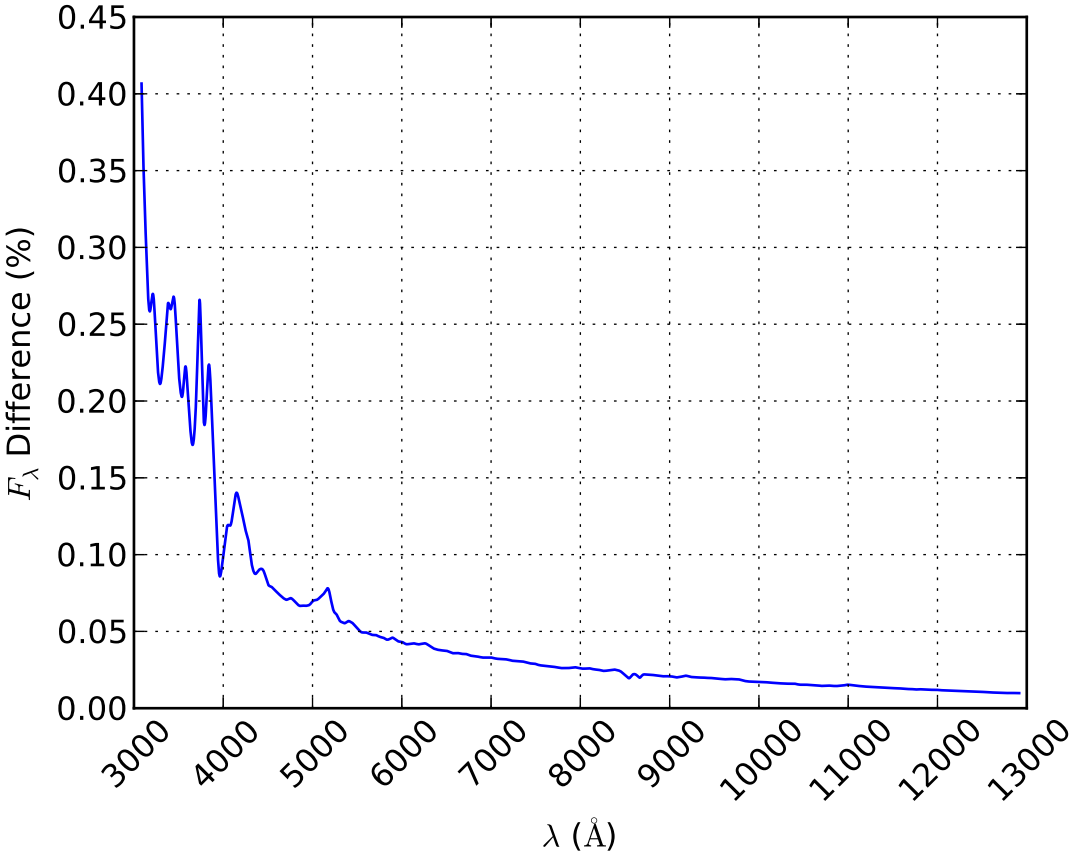

Figure 2.3: Flux distribution difference between SED interpolation methods. Displayed is the difference between linear and logarithmic interpolation between LTE SEDs with $T_{\rm eff}$ = 4700 K and 4750 K to create the LTE SED with $T_{\rm eff}$ = 4725 K.

Table 2.3: 1.5D model components for 1:1 and 2:1 filling factors and resultant 1.5D $T_{\rm eff}$ values

	1:1 Filling Factor			2:1 Filling Factor		
$\Delta T_{1.5\rm D}$(K)	Hot Component $T_{\rm eff}$ (K)	Cool Component $T_{\rm eff}$ (K)	1.5D $T_{\rm eff}$ (K)	Hot Component $T_{\rm eff}$ (K)	Cool Component $T_{\rm eff}$ (K)	1.5D $T_{\rm eff}$ (K)
1050	-	-		4600	3550	4330
1000	4750	3750	4336	-	-	
900	4700	3800	4320	4550	3650	4309
800	4650	3850	4305	-	-	
750	-	-		4500	3750	4292
700	4600	3900	4293	-	-	
600	4550	3950	4281	4450	3850	4277
500	4500	4000	4272	-	-	
450	-	-		4400	3950	4265
400	4450	4050	4264	-	-	
300	4400	4100	4258	4350	4050	4257
200	4350	4150	4254	-	-	
150	-	-		4300	4150	4252
100	4300	4200	4251	-	-	
0	4250	4250	4250	4250	4250	4250

evenly weighting both components for simplicity; and 2) Selecting the components such that $\Delta T_{1.5\rm D}$ be a multiple of 150 K while weighting the hot component at a ratio of 2:1 to the cool component. This ratio represents the relative surface area covered by granules and intergranular lanes respectively (Sheminova 2012). These two methods simulate differences in the temperatures of hot and cool features on the surface of a star, as well as a variation in surface coverage, or filling factor (FF), of the hot and cool features. Hereafter, the evenly weighted method is referred to as having a 1:1 FF, and the method with the hot component being weighted at 2:1 is referred to as having a 2:1 FF. Additionally, two 1.5D control SEDs were created with $\Delta T_{1.5\rm D} = 0$ K, one for each choice of FF. Table 2.3 displays the components used for the two methods, at each $\Delta T_{1.5\rm D}$ that exactly preserves both the $RJ\,T_{\rm eff}$ value as 4250 K and the respective FF, as well as the resultant 1.5D $T_{\rm eff}$ as found from the average of the components' bolometric luminosities.

We attempted to recover the $T_{\rm eff}$ values of the 1.5D stars using three different methods of fitting 1D models: UBVRI photometry, spectrophotometry, and spectroscopy. Common to each method

of post-processing, the 1.5D SEDs were interpolated from their initial wavelength distribution to a new distribution with a constant $\Delta\lambda$ of 0.006 Å. This new $\Delta\lambda$ value was chosen such that all of the spectral lines in each SED remained critically sampled while interpolating to a constant $\Delta\lambda$ wavelength distribution for numerical convenience.

2.2.1 UBVRI photometry

For each of the 1D and 1.5D SEDs, photometric colours were produced using Bessel's updated Johnson-Cousins UBVRI photometry (Bessell 1990). Bessel includes two different B filter response functions, one including atmospheric extinction, B_x, for use with the U filter, and one without, B, for use with the V filter. The transmission data for each filter were interpolated to the wavelength distribution using quadratic splines, as shown in Fig. 2.4. The appropriate regions of each SED were then multiplied by these interpolated filters to acquire transmitted flux spectra that were subsequently integrated over the band-pass region to produce integrated flux values for each filter. Using these integrated flux values, five different colour indices, U_x-B_x, B-V, V-R, V-I, and R-I, were calculated to milli-magnitude precision for each of the SEDs. It should be noted that the U band is of limited accuracy as the short wavelength cutoff in the observational U band is not defined by the instrumental configuration, but rather ozone absorption in Earth's atmosphere. Because ozone column density varies by $\sim$20 % with geographic location and season, it is difficult to accurately reproduce U band photometry synthetically from models. These values were calibrated with a PHOENIX NLTE synthesized SED for the standard star Vega (α Lyr, HR7001, HD172167), using a single-point photometric calibration independent of colour. This was done by applying the same treatment to the Vega 1D SED to calculate colour index values, and applying an offset to the values reducing them to zero. These offset values were applied to the respective colour indices for the rest of the SEDs.

While three of the five colour indices for the 1D SEDs behaved as expected from the behaviour of B_λ, with their values monotonically increasing for decreasing $T_{\rm eff}$ over the range of the 1D SEDs, both the U_x-B_x and B-V indices stopped increasing and started decreasing at $T_{\rm eff}$ = 3900 K for the

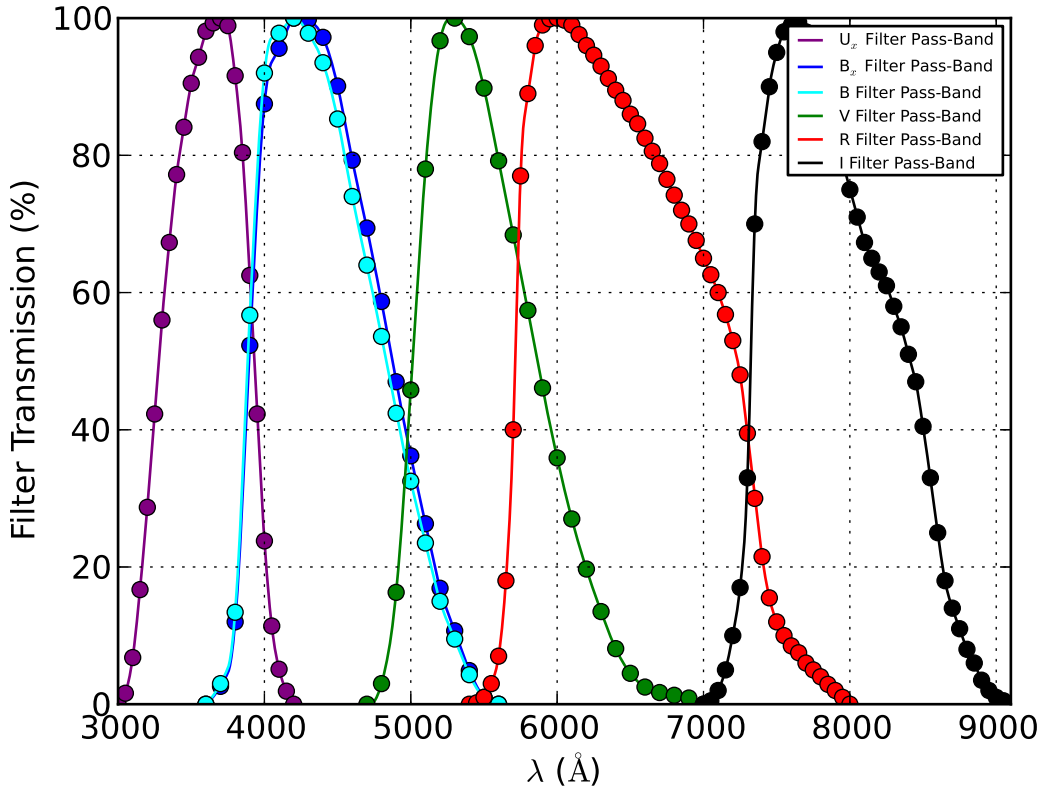

Figure 2.4: Johnson-Cousins UBVRI filter set transmission pass-bands as defined by Bessel. Original filter data with interpolated curves displayed.

LTE SEDs, and at $T_{\rm eff}$ = 3800 K for the NLTE SEDs. This turnover occurs in observed stars, but between $T_{\rm eff}$ = 3540 K and 3380 K for the U-B index (Cox 2000). The phenomenon is caused by spectral features in the B filter growing in strength more rapidly with decreasing $T_{\rm eff}$ than those in the U filter, and reverses the trend in the colour index expected from B_λ. Likewise, the spectral features in the V filter grow more rapidly than those in the B filter. In this case, the incorrect prediction of the $T_{\rm eff}$ value of the turnover is caused by the excess blue and UV flux common to PHOENIX models of cool red giant stars (Short & Hauschildt 2003). Fig. 2.5 shows the B-V index value trend, including turnover, for both the LTE and NLTE 1D SEDs.

The library of 1D colour index values was compared with each of the 1.5D colour index values to find the closest matching $T_{\rm eff}$ value by means of inspection. Whichever 1D SED had the smallest difference between its value and the 1.5D value for each index was chosen as the match. For example, Fig. 2.5 shows the value of the B-V index for the1.5D SED of 1:1 FF with $\Delta T_{\rm 1.5D} =$ 1000 K including the region of closest match to 1D B-V values. Because of the degeneracy caused by the turnover in the U_x-B_x and B-V indices and the limiting numerical resolution of the 1D $T_{\rm eff}$ grid, it was possible that the best matching $T_{\rm eff}$ value would fall outside of the range of temperatures enclosed by the cool and hot 1D components, and would not be the correct match. Because automatically limiting the best match to within the components' $T_{\rm eff}$ range was restrictive, the closest three matches for both of the indices were found and ranked in order, whereupon the correct best match was chosen by inspection to logically fit the $T_{\rm eff}$ range.

2.2.2 Spectrophotometry and Spectroscopy

Absolute surface fluxes of the 1.5D models were comparedWhile the absolute surface fluxes were compared to find the closest match to the the total energy radiated by the 1.5D stars following the spectrophotometric method, the relative fluxes were also compared to find the closest match to the overall shape of the 1.5D SEDs. Taking a spectroscopic approach, rectified spectra were compared to determine the closest match based upon the relative strength of the spectral features.

For the spectrophotometric relative fluxes, the surface flux values were scaled relative to the

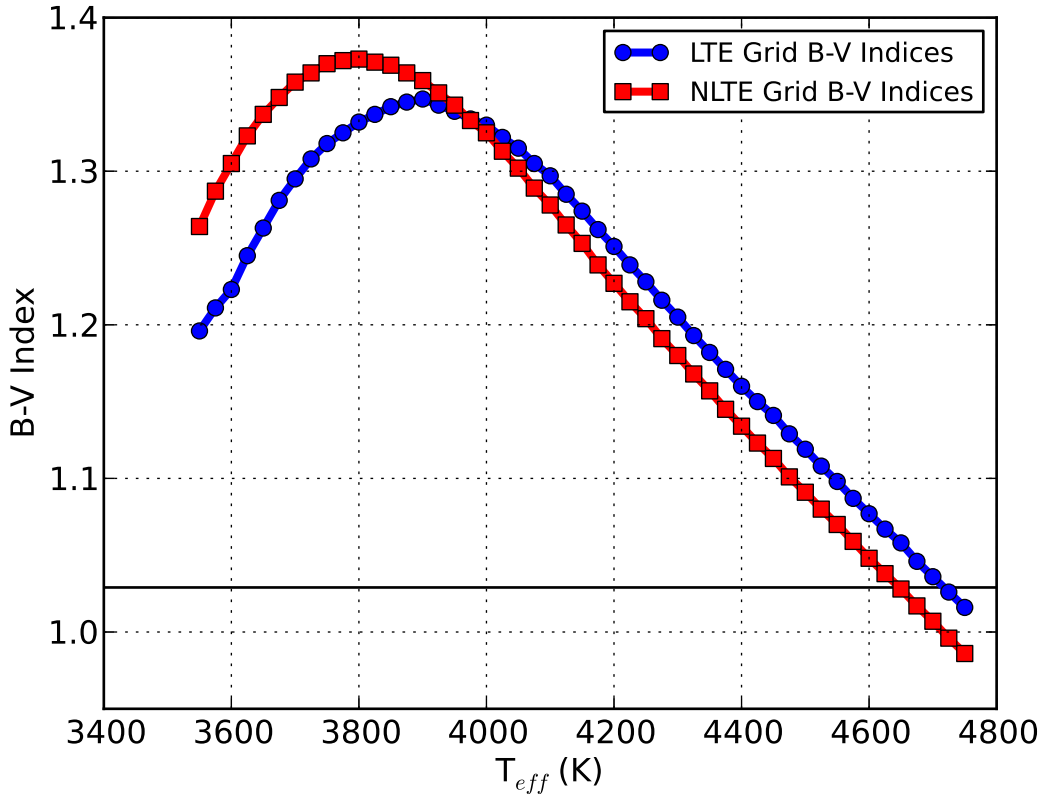

Figure 2.5: B-V colour index values for the LTE and NLTE 1D SEDs. The turnover occurs at $T_{\rm eff}$ = 3900 K for the LTE SEDs and at $T_{\rm eff}$ = 3800 K for the NLTE SEDs. The solid black line indicates the value of the B-V index for the $\Delta T_{\rm 51D} = 1000$ K, 1:1 FF 1.5D SED.

average flux within a 10 Å window ($F_{\rm window}$) located between $\lambda = 12750$ Å and 12760 Å in the Rayleigh-Jeans tail of each SED, the "pinning" point. A 10 Å window was chosen over a single data point to avoid having selected a point that unreliably represents the total flux level relative to the continuum level in different SEDs because, for example, of being placed at the location of a spectral line. Additionally, this window was chosen over others in the Rayleigh-Jeans tail because, among all of the 1D SEDs, it regularly had the fewest and weakest spectral features contained within its bounds compared to all other windows at wavelengths longer than $\lambda = 11000$ Å. Fig. 2.6 displays the pinned version of the NLTE SEDs with $T_{\rm eff}$ values of 4750 K, 4250 K, and 3550 K..

To assess the strength of spectral features spectroscopically, the shape of the continuum needs to be removed from the SED. This rectification was done for the 1D spectra by dividing the blanketed spectra by the corresponding continuum spectra. For the 1.5D SEDs, the same rectification process was used, but the 1.5D synthetic continua were generated the same way that the 1.5D SEDs were, by linearly averaging the two corresponding synthetic continua together. A high resolution, line blanketed rectified spectrum for the NLTE SED with $T_{\rm eff}$ = 4250 K overlaid with its own convolved rectified spectrum is presented in Fig. 2.7. Two different estimates of the best fitting $T_{\rm eff}$ value were obtained for each 1.5D SED with this method. One for the entire wavelength range, and another by restricting the fit to the wavelength range between $\lambda = 5500$ Å and 8000 Å. This range was selected to isolate the distinctive TiO molecular absorption bands present in cool star spectra (Davies et al. 2013). A MgH band centered at 5167 Å was found to overlap with the TiO band near this wavelength range, and depended differently on $T_{\rm eff}$ than the TiO bands, affecting the quality of the fits. The overlapping MgH and TiO bands and additional nearby TiO bands are displayed in Fig. 2.8, illustrating the different temperature dependence of the features.

To prepare the data for calculating the best fits, each of the high resolution 1D and 1.5D SEDs were convolved with a Gaussian kernel having a FWHM of 50 Å, representing the nominal resolution element of the observed spectrophotometry in the Burnashev catalogue Burnashev (1985). The smoothed SEDs were then re-sampled to a much coarser $\Delta\lambda$ spacing to more accurately reflect the number of degrees of freedom available when comparing with an observed SED, but still fine

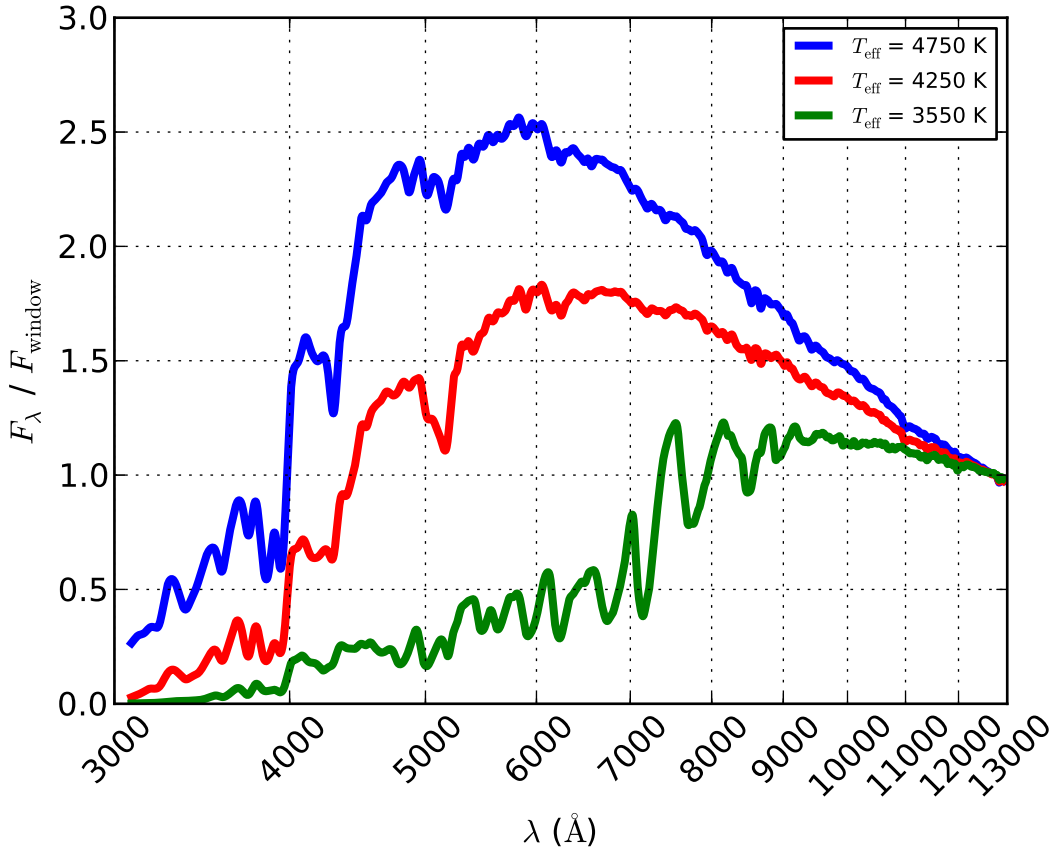

Figure 2.6: Pinned version of three NLTE SEDs with $T_{\rm eff}$ values of 4750 K, 4250 K, and 3550 K.

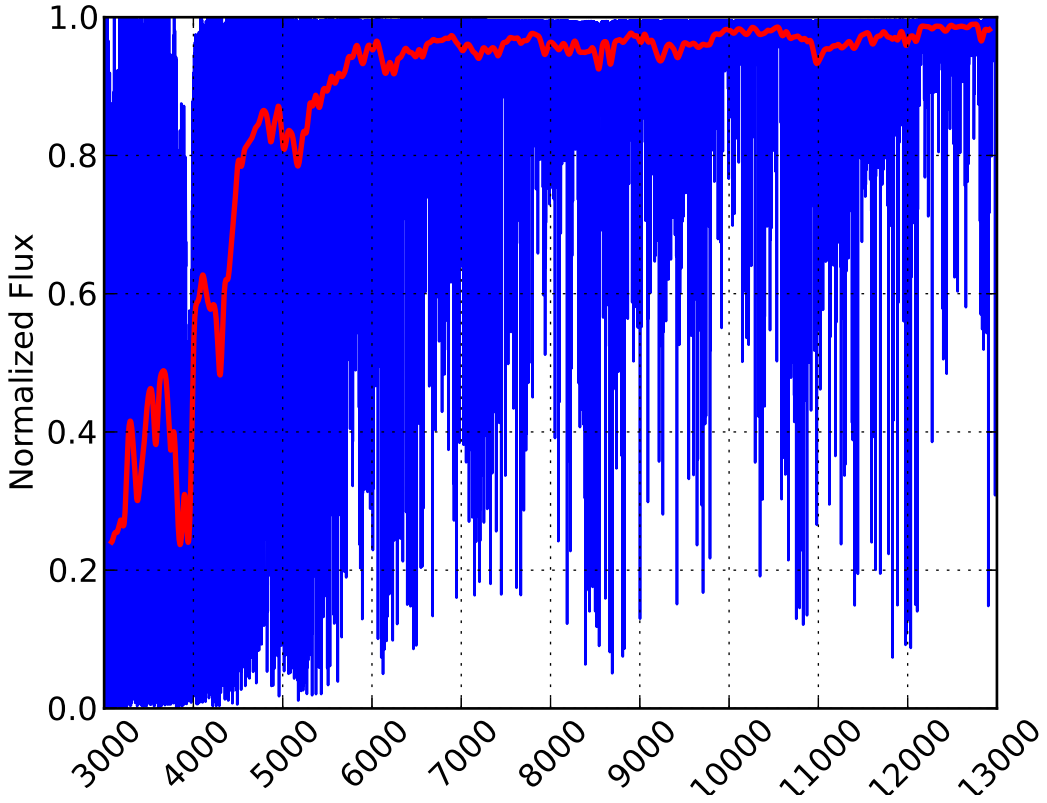

Figure 2.7: Rectified spectra for the $T_{\rm eff}$ = 4250 K NLTE SED. The high resolution line blanketed rectified spectrum is displayed in blue; the red overlay is the rectified spectrum smoothed with the 50 Å FWHM Gaussian.

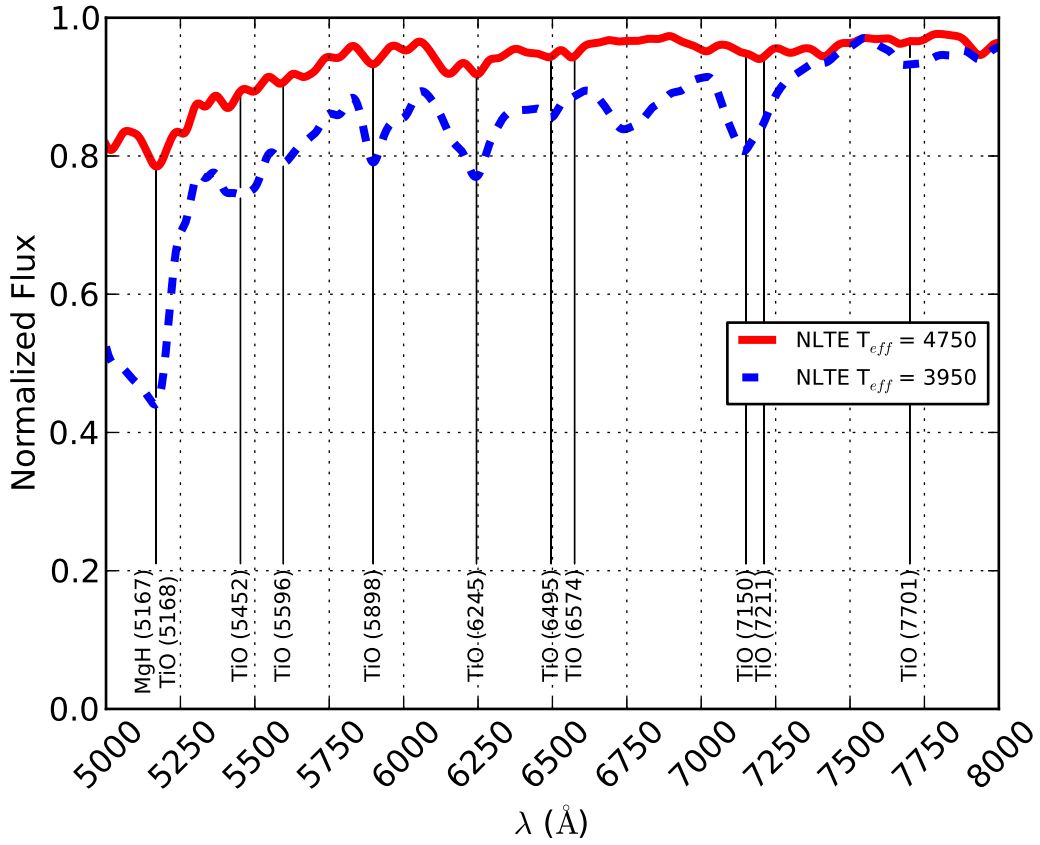

Figure 2.8: Flattened NLTE 1D spectra with $T_{\rm eff} = 4750$ K and 3950 K, restricted to a wavelength range of $\lambda = 5000$ Å to 8000 Å. Strong molecular absorption features in the region have been identified to illustrate the difference in temperature dependence of the MgH and TiO features.

enough to critically sample every feature remaining after the smoothing convolution. This amounted to a sample of 4000 wavelength points spaced between $\lambda = 3100$ Å and 12900 Å, with 100 Å at each end of the original wavelength range having been lost to convolution edge effects. For both spectrophotometric approaches, the new points were evenly distributed in logarithmic space instead of linear space, amounting to taking the log of the upper and lower bounds of the wavelength region, distributing the new sample points evenly between these values, and then exponentiating everything to return to linear space. This resulted in a distribution of wavelength points with smaller $\Delta\lambda$ at shorter wavelengths and larger $\Delta\lambda$ at longer wavelengths. The motivation behind this was to attribute additional weight to spectral features located in the blue end of the SED when determining a best fit, without arbitrarily weighting select wavelength regions more heavily or determining a best fit for these regions separate from the rest of the SED altogether. Extra weighting was attributed to the blue band of the wavelength range because there are more spectral features per $\Delta\lambda$ interval there, and it is more sensitive to changes in temperature than the red band, making it a more sensitive diagnostic tool for determining $T_{\rm eff}$. The rectified spectra of the spectroscopic approach were re-sampled in linear wavelength space to not grant any of the spectral features additional weight in the final fitting process. Unlike the spectrophotometric SEDs, the relative strengths of individual spectral features are what is of interest here, not the overall shape of the spectrum.

In all cases, the best fit 1D spectrum was determined by minimizing a modified Pearson χ^2 test statistic. The Pearson χ^2 test statistic is of the form

$$\chi^2 = \frac{1}{n}\sum_{i=1}^{n}\frac{(O_i - M_i)^2}{M_i}, \tag{2.1}$$

where n is the number of degrees of freedom, O_i is the observed frequency of a phenomenon to be fitted, and M_i is the modelled or expected frequency of the phenomenon. The 1D and 1.5D fluxes were treated as the modelled and observed frequencies, because a spectral flux is in some sense the frequency at which photons of given energies emerge from stars. The modified form of the test statistic used here involved comparing the ratio of the 1D and 1.5D fluxes by way of

$$\chi^2 = \frac{1}{n}\sum_{i=1}^{n}\frac{(1 - M_i/O_i)^2}{M_i/O_i}. \tag{2.2}$$

For each 1.5D SED, every 1D SED was individually treated as the model value to create a test statistic value. The 1D SED with the minimum χ^2 value was chosen as the best fitting SED from which the 1.5D $T_{\rm eff}$ was inferred. In each fitting case, the result was determined to be significant at a confidence level of $p = 0.05$. Fig. 2.9 displays the χ^2 curves for the 1000 K contrast, even FF 1.5D SED. As a check for self consistency, the 1D NLTE fitted results are expected to be bounded by the hot and cold components' $T_{\rm eff}$ values for a given 1.5D star, but this restriction is not expected of the 1D LTE fitted results.

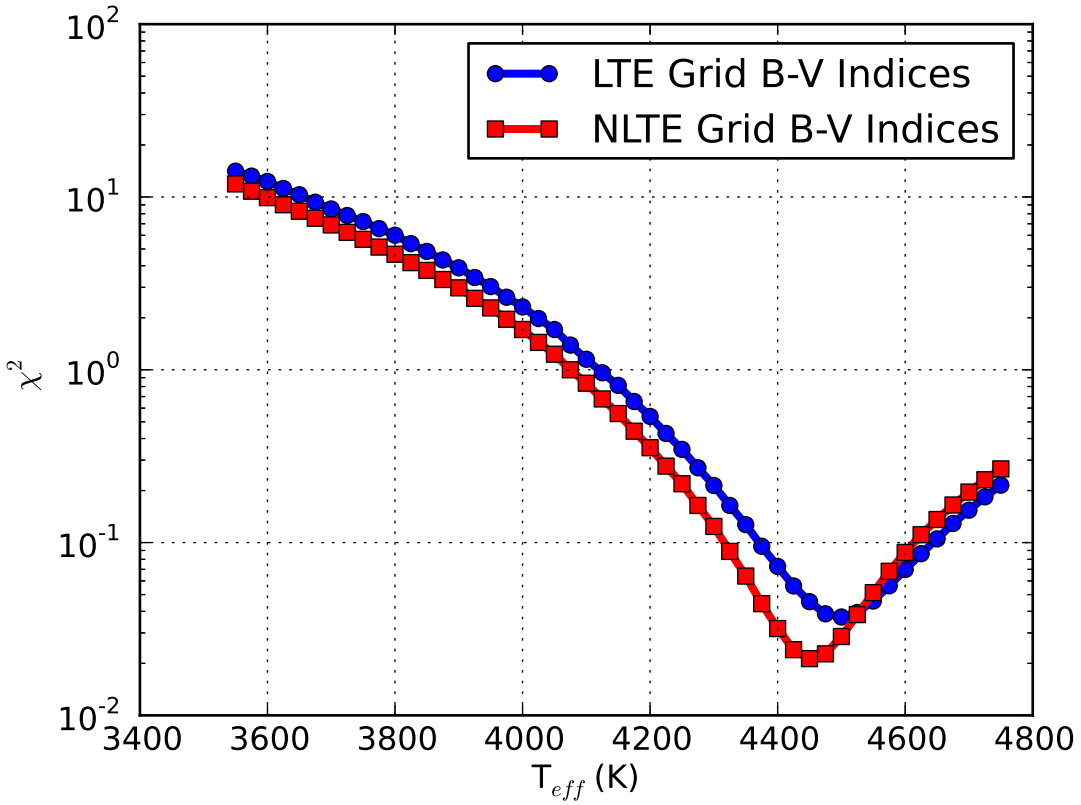

Figure 2.9: The χ^2 curves for the 1000 K, 1:1 filling factor, 1.5D SED for both the LTE and NLTE 1D SEDs.

Chapter 3

Results of 1D $T_{\rm eff}$ Fitting

In all cases except one, the best fitting $T_{\rm eff}$ values for the 1.5D stars showed an increasing trend with increasing $\Delta T_{\rm 1.5D}$. This is expected from the non-linear dependence of B_λ on temperature, where a hotter $T_{\rm eff}$ value produces disproportionately more flux than a cooler one, and the averaged flux in 1.5D stars will be more than a $T_{\rm eff}$ value of 4250 K would suggest for a 1D star. This effect is even more pronounced at bluer wavelengths. Taking the derivative of B_λ with respect to temperature,

$$\frac{\partial B_\lambda}{\partial T} = \frac{2h^2c^3}{\lambda^6 k_B T_{\rm eff}^2} \frac{e^{\frac{hc}{\lambda k_B T}}}{\left(e^{\frac{hc}{\lambda k_B T}} - 1\right)^2}, \tag{3.1}$$

inspection reveals that for changing temperatures, B_λ exhibits larger relative changes at shorter wavelengths, causing the flux at the blue end of the spectrum to increase disproportionately faster than the rest of the wavelength range with increasing $T_{\rm eff}$.

In the case of the TiO bands fitted in the rectified spectra, the reverse trend was instead seen; a decreasing best fit $T_{\rm eff}$ with increasing $\Delta T_{\rm 1.5D}$. This is expected from the non-linear dependence of molecule formation on gas temperature (Uitenbroek & Criscuoli 2011). All fitting results are considered as having a formal uncertainty of $\delta T = \pm 25$ K, one half of the original numerical temperature resolution of the 1D grid, representing that these are closest fitting $T_{\rm eff}$ values, not exact

fit $T_{\rm eff}$ values. The results are summarized in Tables 3.1 and 3.2 at the end of the chapter.

3.1 UBVRI photometry

Fig. 3.1 presents each of the five photometric color indices' NLTE best fitting $T_{\rm eff}$ values as a function of $\Delta T_{\rm 1.5D}$ for all of the 1.5D stars. Each of the color indices shows increasing best fit $T_{\rm eff}$ values for the 1.5D stars with increasing $\Delta T_{\rm 1.5D}$. The slope of the $T_{\rm eff}$ $(\Delta T_{\rm 1.5D})$ relation is different for the five indices, creating, for a given 1.5D star, a spread of best fit $T_{\rm eff}$ values among the indices that grows with increasing $\Delta T_{\rm 1.5D}$. The slopes of the individual colour indices' fits are steeper for the bluer indices, and nearly flat for the R-I index over the $\Delta T_{\rm 1.5D}$ range. Such a spread in the fits shows that horizontal inhomogeneity effects are non-constant across the spectrum. This spread cannot be resolved at a 25 K resolution for $\Delta T_{\rm 1.5D} \leq 150$ K, and grows as large as 375 K for 1.5D stars with 1:1 FF, and as large as 250 K for 2:1 FF. Eq. 3.1 confirms that colour indices at shorter wavelengths should be more dependent on $\Delta T_{\rm 1.5D}$.

For the 2:1 FF fits, the spread is not as large as the 1:1 FF because, while the 2:1 1.5D star is created with more hot material than cool material, the $T_{\rm eff}$ values of both components are lower than the respective components of a 1:1 1.5D star having the same $\Delta T_{\rm 1.5D}$, outweighing the contribution of more hot material by having less flux to contribute from the hot component. This resulted in either the same or lower temperature fits for a given $\Delta T_{\rm 1.5D}$. Additionally, because the cool component of the 2:1 1.5D stars has a lower $T_{\rm eff}$ value than that of a 1:1 1.5D star, the blue and UV regions are even more severely line-blanketed, contributing even less flux than the $T_{\rm eff}$ difference alone would suggest, and resulting in lower temperature fits for the colour indices at shorter wavelengths, noticeably U_x-B_x and B-V.

To quantify the magnitude of NLTE effects, we defined the quantity $\Delta T_{\rm NLTE}$ as the difference between the fitted NLTE $T_{\rm eff}$ value and the fitted LTE $T_{\rm eff}$ value for a 1.5D star. Examining each colour index individually for the effects of NLTE, it is seen in Figs. 3.2, 3.3, and 3.4 that both choices of FF return LTE best fit $T_{\rm eff}$ values that are always hotter than the NLTE best fits for a given $\Delta T_{\rm 1.5D}$,

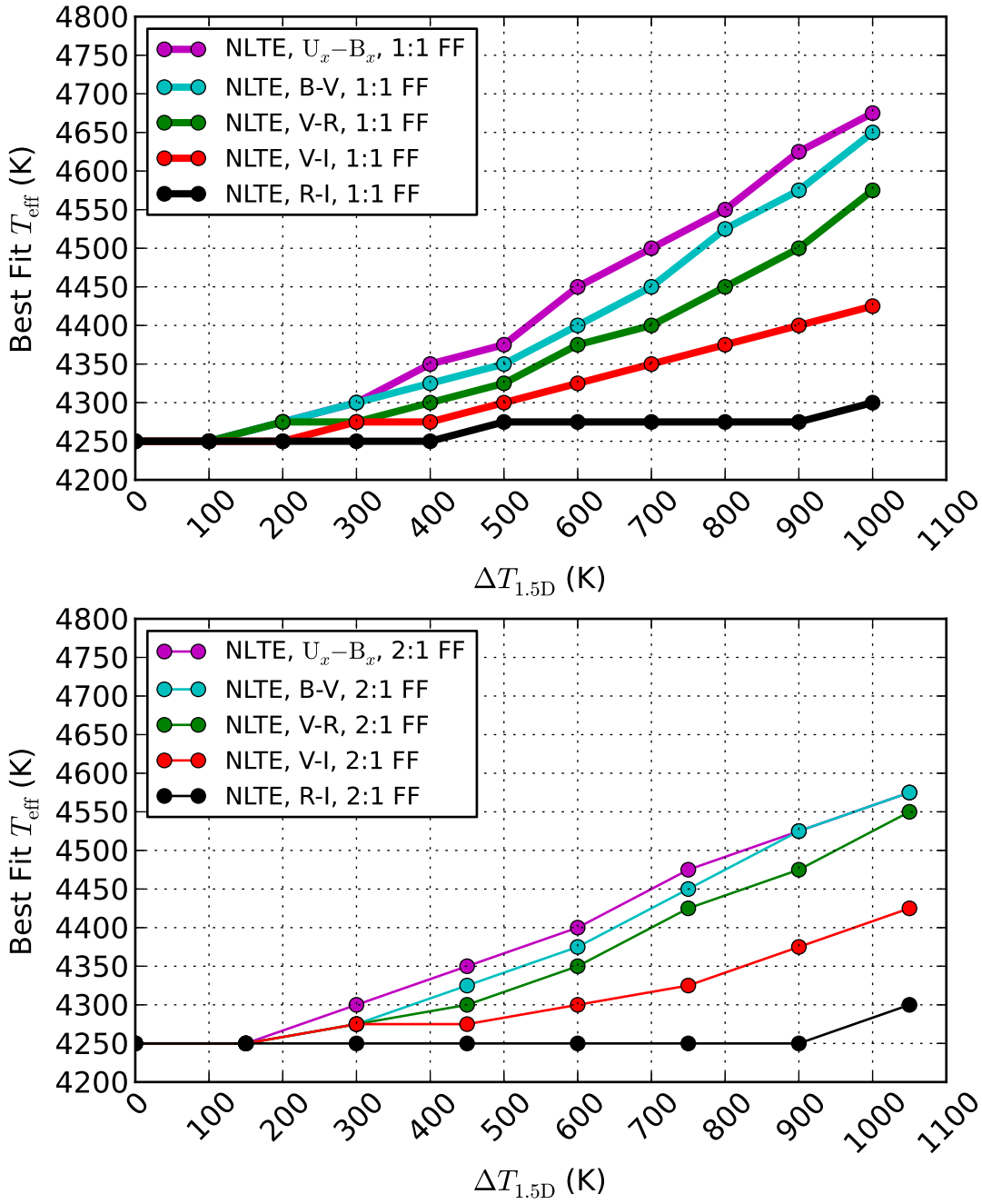

Figure 3.1: Inferred $T_{\rm eff}$ values for five photometric colour indices. The top image displays results for the 1:1 FF, the bottom displays results for the 2:1 FF.

and that $\Delta T_{\rm NLTE}$ is approximately constant withing one numerical temperature resolution unit for all choices of $\Delta T_{\rm 1.5D}$ for each colour index. This constant value depends on colour index, suggesting that NLTE effects are non-constant across the spectrum, but they are temperature independent over the range of $T_{\rm eff}$ values in the 1D grid. For the U_x-B_x index, the magnitude of $\Delta T_{\rm NLTE}$ is at least 100 K larger than the other indices because of the greater flux in the blue and UV from NLTE Fe I overionization, forcing the LTE SEDs to have a higher $T_{\rm eff}$ value to match the flux. Fig. 3.2 displays the results for the U_x-B_x index, showing a nearly constant value for $\Delta T_{\rm NLTE}$ of -150 K to -175 K. The plateau in the LTE 1:1 FF $T_{\rm eff}$ $(\Delta T_{\rm 1.5D})$ relation above $\Delta T_{\rm 1.5D} = 800$ K is not a breaking of this constant $\Delta T_{\rm NLTE}$, but rather the best fit $T_{\rm eff}$ values were restricted by the upper limit of the 1D grid of models. Fig. 3.3 and Fig. 3.4 display the results for the remaining colour indices, each of which having a magnitude of $\Delta T_{\rm NLTE}$ of 75 K or less. The irregularity of the dip in the R-I index fits for the 2:1 FF 1.5D stars is numerical. The variation in R-I colours for the 1D and 1.5D stars occurred at the milli-magnitude level, which was the limiting resolution of the photometric colour calculations.

3.2 Spectrophotometry

3.2.1 Absolute Flux SEDs

Fig. 3.5 presents the results of fitting 1D NLTE absolute SEDs to the 1.5D absolute SEDs for both choices of FF. Both choices of FF show an increasing trend in best fitting $T_{\rm eff}$ values for increasing $\Delta T_{\rm 1.5D}$. For values of $\Delta T_{\rm 1.5D} \leq 300$ K, both choices of FF produce the same best fitting $T_{\rm eff}$ value for a given $\Delta T_{\rm 1.5D}$ value, whereas for values of $\Delta T_{\rm 1.5D} \geq 400$ K, the 1:1 FF 1.5D SEDs produce hotter $T_{\rm eff}$ values than the 2:1 FF SEDs. The 1:1 FF SEDs reached a best fitting $T_{\rm eff}$ value of 4450 K and the 2:1 FF SEDs reached 4425 K at maximum $\Delta T_{\rm 1.5D}$. Fig. 3.6 shows the 1.5D 1:1 FF SED with $\Delta T_{\rm 1.5D} = 1000$ K plotted with the best fitting 1D NLTE SED and two bracketing 1D NLTE stars. While the 1.5D star is statistically matched to the 1D star having the closest absolute total flux value, it can be seen that the 1.5D stars redistribute the flux across the λ range, increasing the flux in

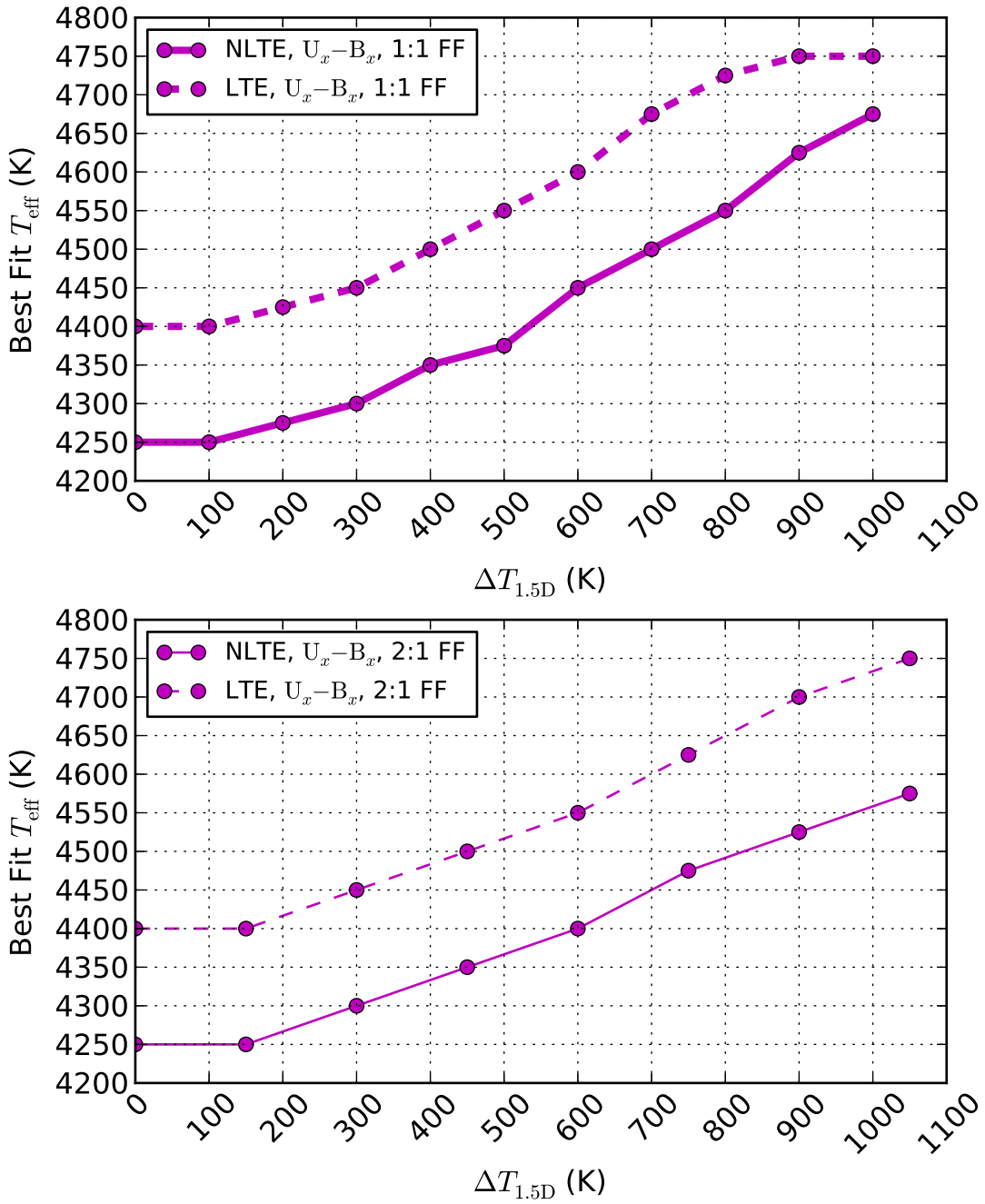

Figure 3.2: U_x-B_x index best fit $T_{\rm eff}$ value results. The top image contains results for 1.5D stars with 1:1 FF, while the bottom image contains those for 2:1 FF. Results from NLTE (solid lines) and LTE (dashed lines) 1D modelling. The data points for the LTE 1:1 FF fits at $\Delta T_{\rm 1.5D} = 900$ K and 1000 K are at the upper limit of the 1D grid of models and may not accurately represent what the best fitting $T_{\rm eff}$ values may be.

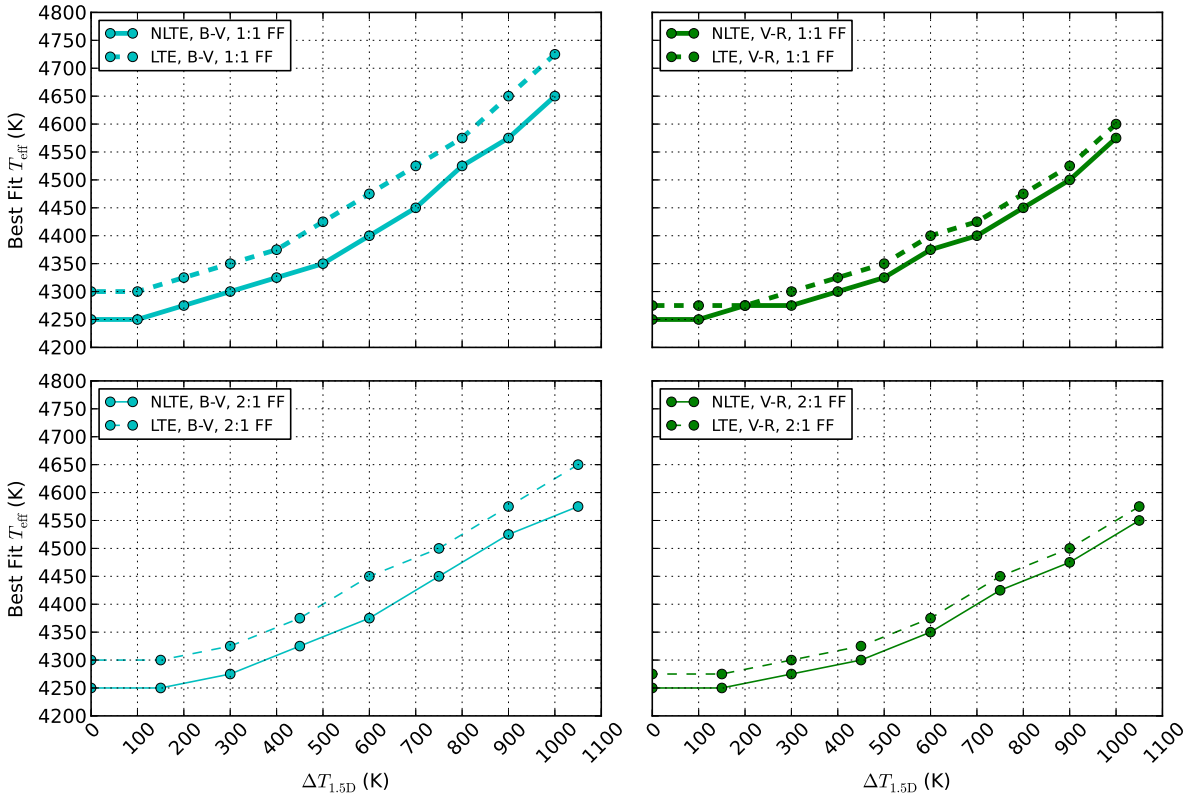

Figure 3.3: Same as Fig. 3.2, but for B-V and V-R indices.

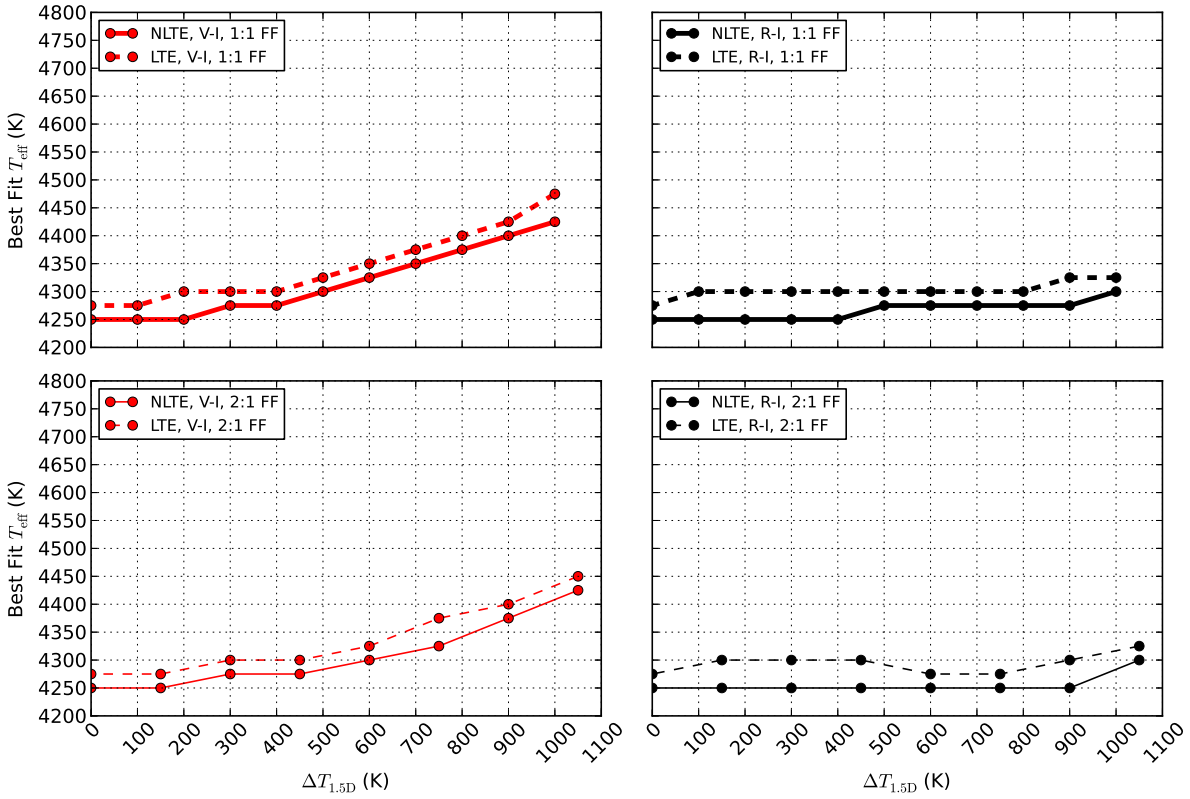

Figure 3.4: Same as Fig. 3.2, but for V-I and R-I indices.

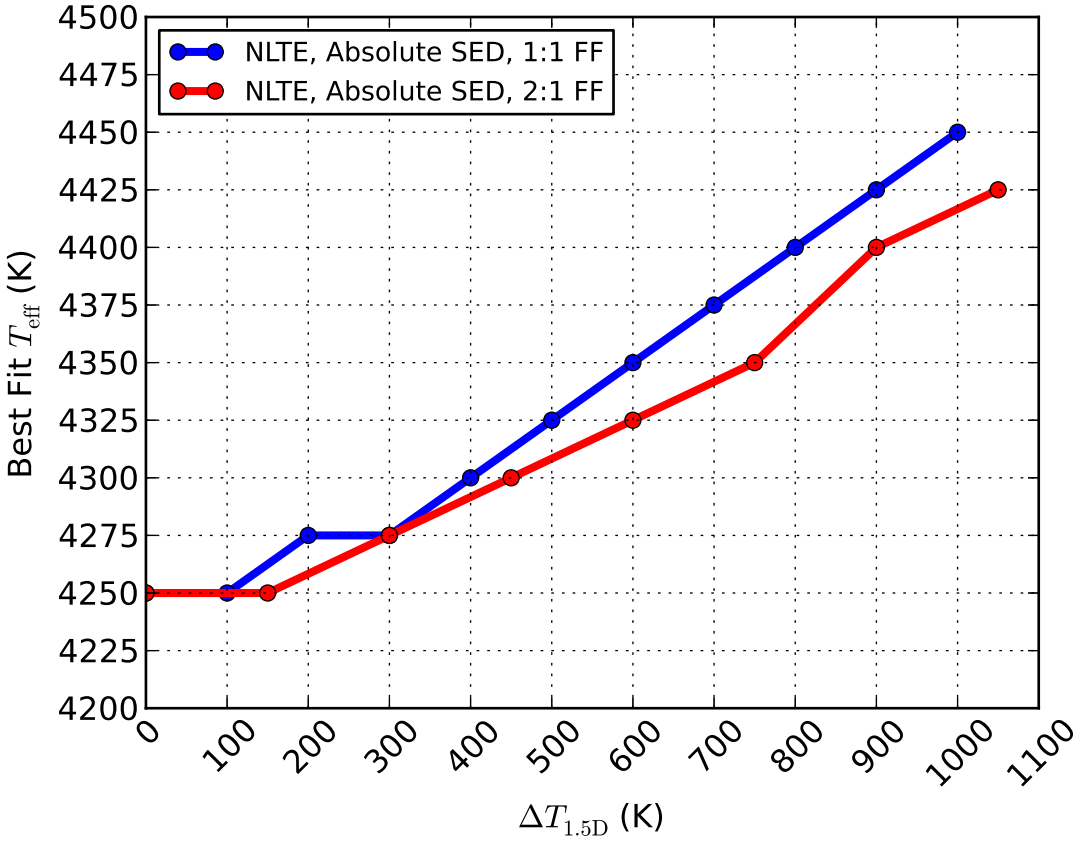

Figure 3.5: Inferred $T_{\rm eff}$ from fitting Absolute Flux SEDs with 1D NLTE models.

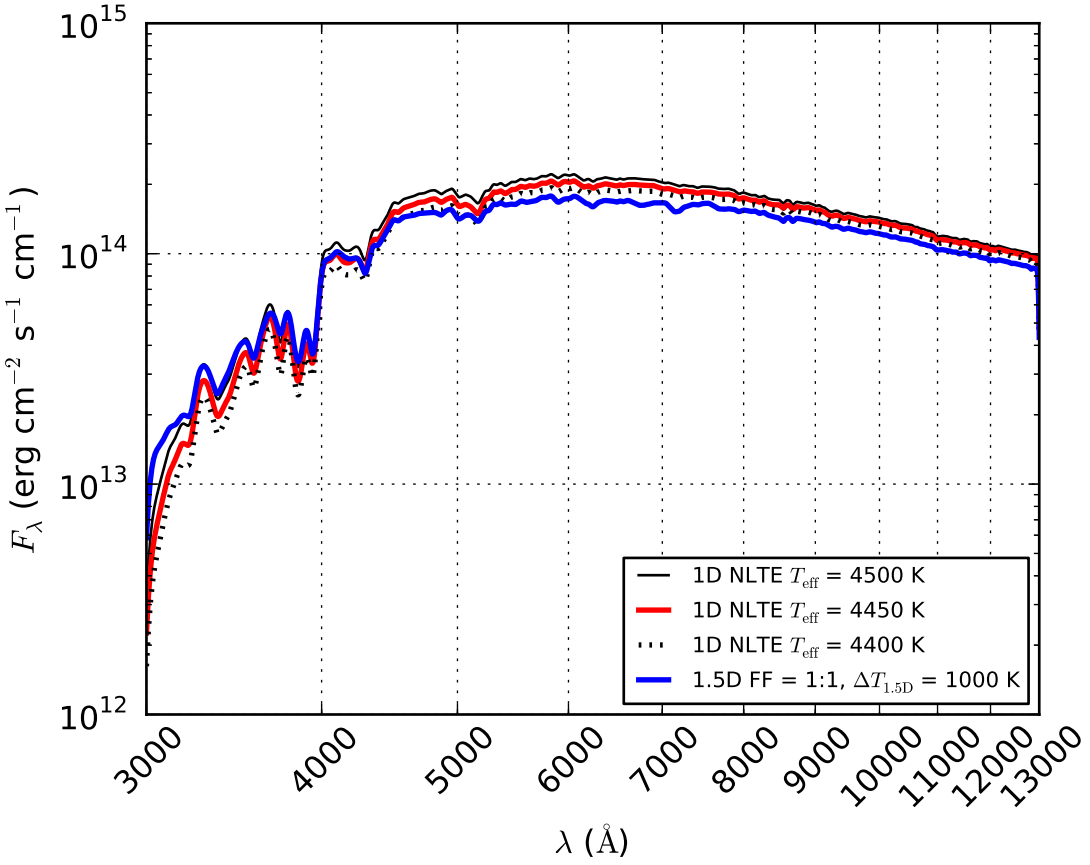

Figure 3.6: Absolute Flux 1.5D 1:1 FF SED (blue) with the best fitting 1D NLTE SED (red) and additional 1D NLTE SEDs (black) spaced two temperature resolution units ($\Delta T_{\rm eff} = 50$ K) above and below the best fitting 1D SED for comparison.

the Wein regime, and decreasing it in the Rayleigh-Jeans tail. In both the Wein and Rayleigh-Jeans regimes this redistribution alters the spectrum to the extent that the difference between the 1.5D SED and best fitting 1D SED is greater than the difference between adjacent 1D SEDs.

Fig. 3.7 displays the LTE results compared with the NLTE results for both choices of FF. In both cases, and for every value of $\Delta T_{\rm 1.5D}$, the LTE best fitting $T_{\rm eff}$ values are hotter than the NLTE values. Because NLTE stars produce more blue and UV flux for a given $T_{\rm eff}$ value than LTE stars, the LTE 1D SEDs returned higher best fitting $T_{\rm eff}$ values to match the absolute flux value of the 1.5D SED. For the 1:1 FF 1.5D SEDs, $\Delta T_{\rm NLTE}$ varied between 25 K and 50 K, whereas for the 2:1 FF SEDs, $\Delta T_{\rm NLTE}$ was nearly constant at 50 K, only dropping to 25 K for $\Delta T_{\rm 1.5D} = 900$ K.

3.2.2 Relative Flux SEDs

The results of fitting 1D NLTE relative flux SEDs to the 1.5D SEDs are presented in Fig. 3.8. Both choices of FF show an increasing trend in best fitting $T_{\rm eff}$ values for increasing $\Delta T_{\rm 1.5D}$ with the 1:1 FF best fitting $T_{\rm eff}$ values being hotter than the 2:1 best fits at every value of $\Delta T_{\rm 1.5D} > 100$ K. The 1:1 FF SEDs reached a best fitting $T_{\rm eff}$ and the 2:1 FF SEDs reached 4475 K at maximum $\Delta T_{\rm 1.5D}$. Fig. 3.9 displays the 1.5D 1:1 FF relative SED with $\Delta T_{\rm 1.5D} = 1000$ K plotted with the best fitting 1D NLTE relative SED and two bracketing 1D NLTE stars. Because the logarithmically spaced λ grid was utilized to place more weight on bluer wavelengths for the fits, the 1.5D SED matches well with the best fitting 1D SED for $\lambda \lesssim 4500$ Å, but the 1D SED fails to predict the shape of the 1.5D SED around the peak of the spectrum; here, the 1.5D SED would be fit by a SED with less flux at these wavelengths relative to $F_{\rm window}$, suggesting a cooler $T_{\rm eff}$ value for the best fitting 1D SED. That the 1.5D and 1D SEDs appear to match up closely again in the R-J tail is inconsequential; all of the relative flux SEDs are normalized to the same 10 Å window and are expected to converge near this point. Both the LTE and NLTE results are presented in Fig. 3.9 broken down by FF. The LTE best fitting $T_{\rm eff}$ values are hotter than the NLTE values for every value of $\Delta T_{\rm 1.5D}$. For both choices of FF, $\Delta T_{\rm NLTE}$ varied between 50 K and 75K.

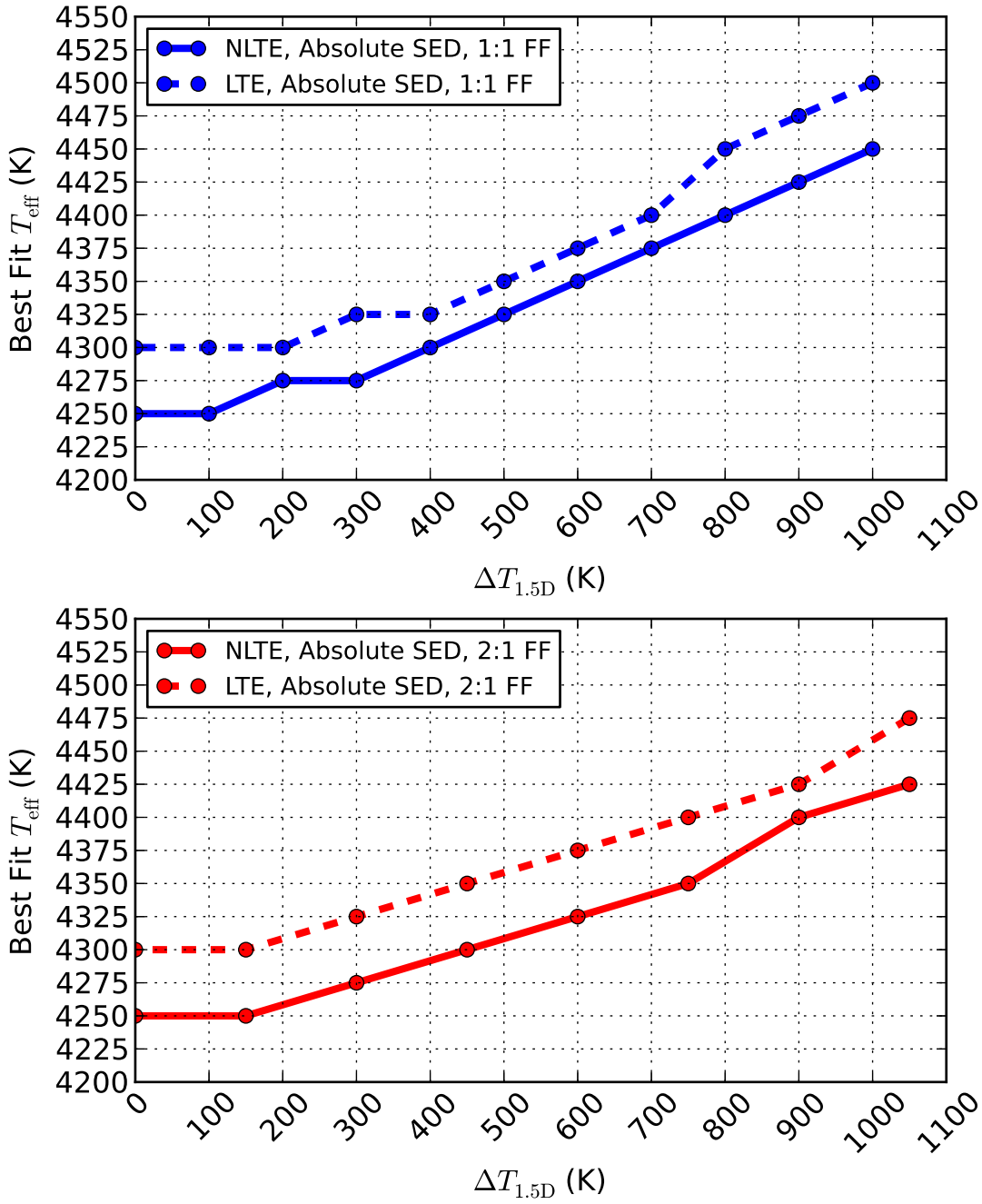

Figure 3.7: Inferred $T_{\rm eff}$ from fitting Absolute Flux SEDs with NLTE (solid lines) and LTE (dashed lines) 1D models.

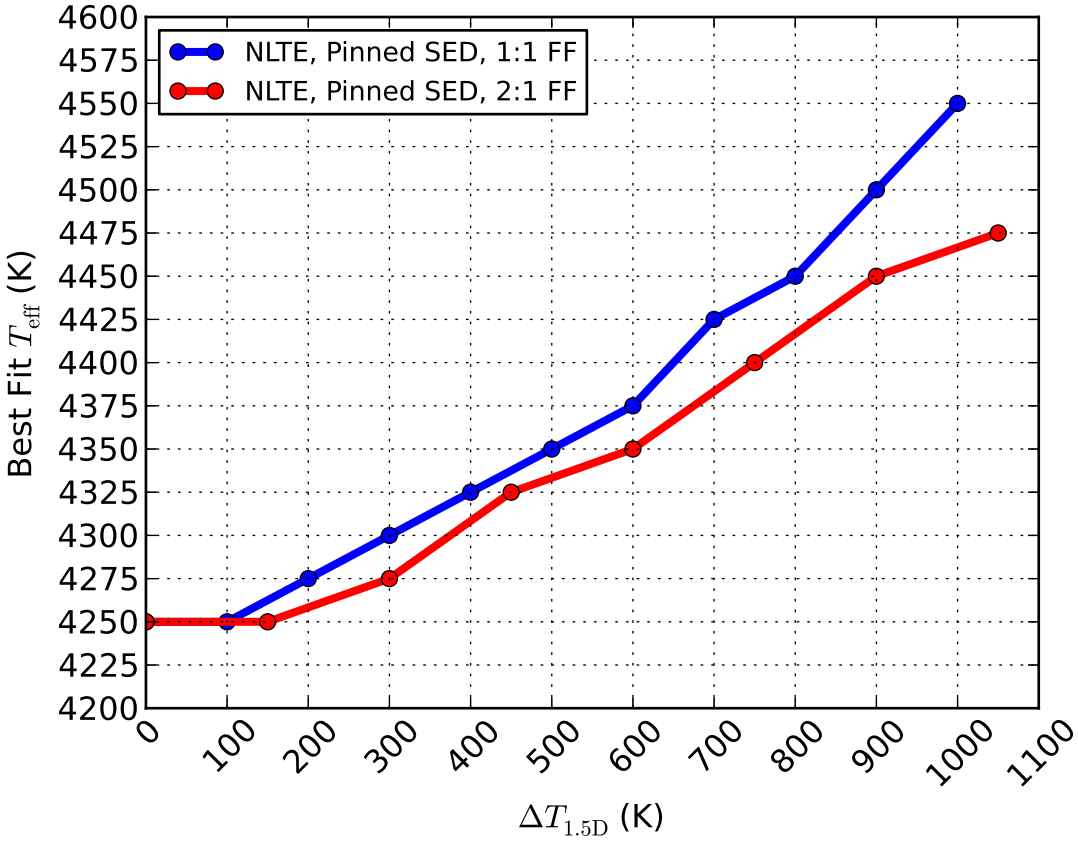

Figure 3.8: Same as Fig. 3.5, but for pinned SEDs.

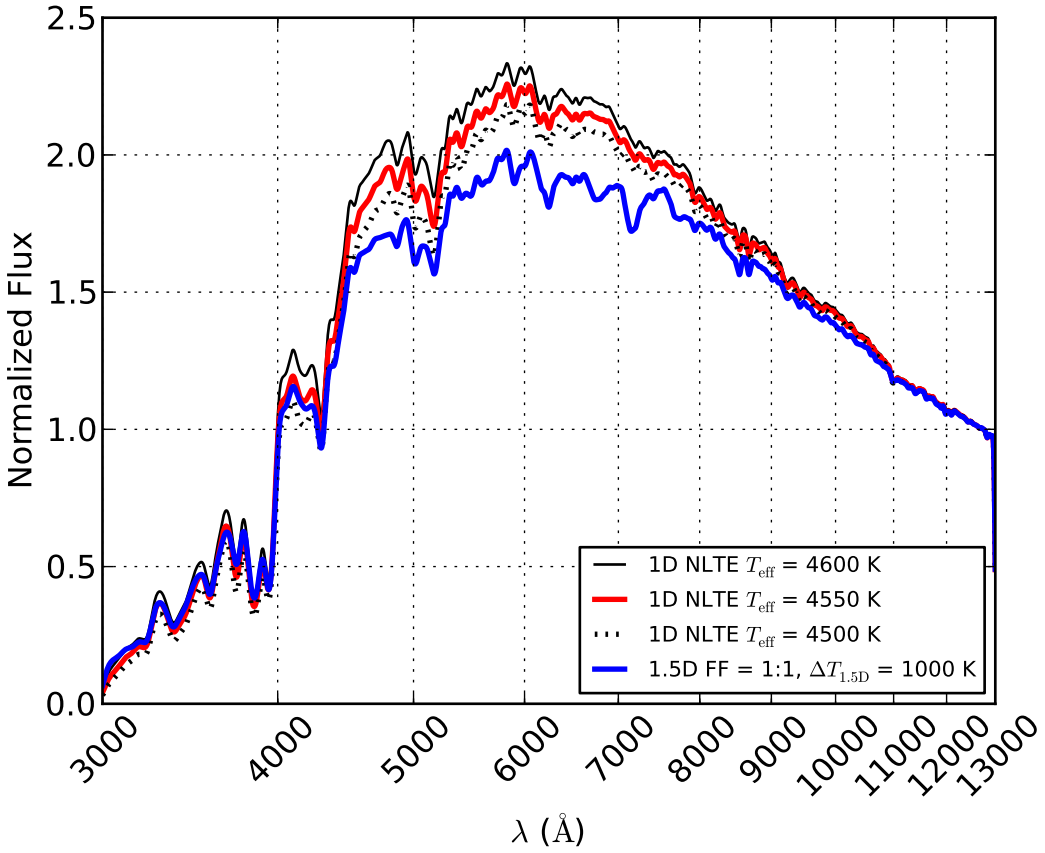

Figure 3.9: Same as Fig. 3.6 but for Pinned SEDs

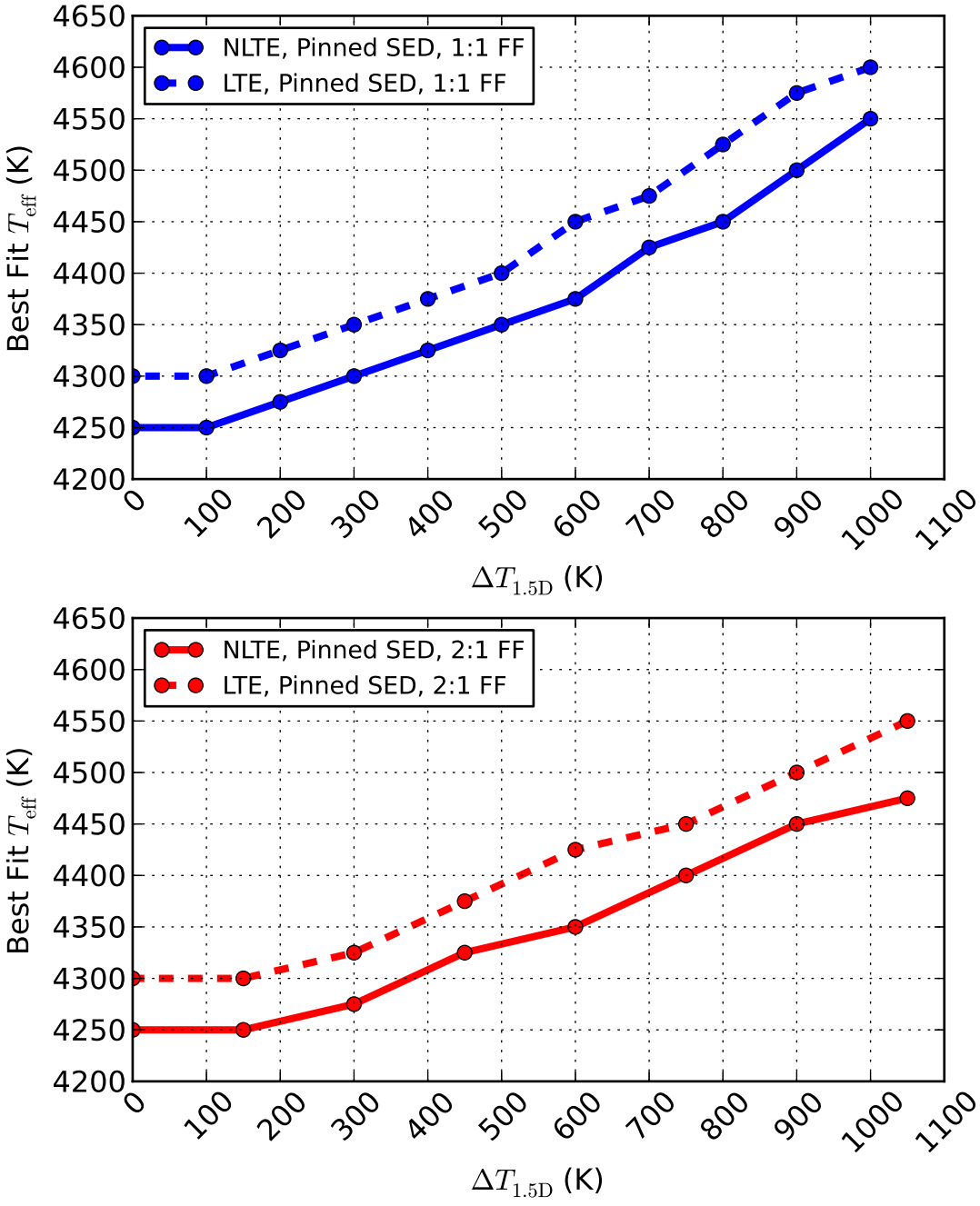

Figure 3.10: Same as Fig. 3.7, but for pinned SEDs.

3.3 Spectroscopy

Fig. 3.11 displays the NLTE best fitting $T_{\rm eff}$ values from fitting rectified spectra over the entire λ range for all of the 1.5D stars. The best fit $T_{\rm eff}$ values below $\Delta T_{\rm 1.5D} = 500$ K are approximately equal at each $\Delta T_{\rm 1.5D}$ for both choices of FF, and only begin to differ above $\Delta T_{\rm 1.5D} = 600$ K, with the 1:1 FF 1.5D stars having hotter fitted values. The inequality reaches a maximum $T_{\rm eff}$ value difference of 100 K at the maximum $\Delta T_{\rm 1.5D}$, with the 1:1 FF 1.5D stars reaching a maximum $T_{\rm eff}$ value of 4650 K.

Fig. 3.12 shows the 1.5D 1:1 FF rectified spectrum with $\Delta T_{\rm 1.5D} = 1000$ K plotted with the best fitting 1D NLTE spectrum and two bracketing 1D NLTE spectra. The best fitting 1D spectrum is seen to be a good fit to the 1.5D spectrum for the blue and red ends of the λ range, but is a poor match between $\lambda \approx 4500$ Å and 8000 Å. In the region, the 1.5D spectrum exhibits stronger spectral features than the best fitting 1D spectrum indicates, suggesting that there is a cooler best fitting $T_{\rm eff}$ value for this region.

Comparing the NLTE results with LTE results, it is seen that for both FF values, the LTE best fit $T_{\rm eff}$ values are hotter than the NLTE fits, but $\Delta T_{\rm NLTE}$ increases with increasing $\Delta T_{\rm 1.5D}$, as shown in Fig. 3.13. For the 2:1 FF 1.5D stars, $\Delta T_{\rm NLTE}$ reaches a maximum of 175 K, and for the 1:1 FF stars, it is potentially even larger but the LTE results plateau above $\Delta T_{\rm 1.5D} = 800$ K, similar to the U_x-B_x photometric colour index in Section 3.1, and for the same reasons.

Fig. 3.14 shows NLTE best fitting $T_{\rm eff}$ values inferred from fitting to rectified spectra restricted to the TiO bands located between $\lambda = 5500$ Å and 8000 Å for all 1.5D stars. A decreasing trend of fitted $T_{\rm eff}$ with increasing $\Delta T_{\rm 1.5D}$ is observed, dropping as low as $T_{\rm eff} = 4000$ K at maximum $\Delta T_{\rm 1.5D}$. This agrees with the observation from Fig. 3.12 that the best fitting $T_{\rm eff}$ values for this λ should be cooler than those found for the same star when fitting the entire visible band. Both of the FF values produce similar results when fit with NLTE 1D stars, the fits being separated by no more than one numerical temperature resolution unit at any $\Delta T_{\rm 1.5D}$. The 1:1 FF 1.5D stars have the hotter fitted $T_{\rm eff}$ values at $\Delta T_{\rm 1.5D}$ values greater than 600 K. The TiO molecular bands grow

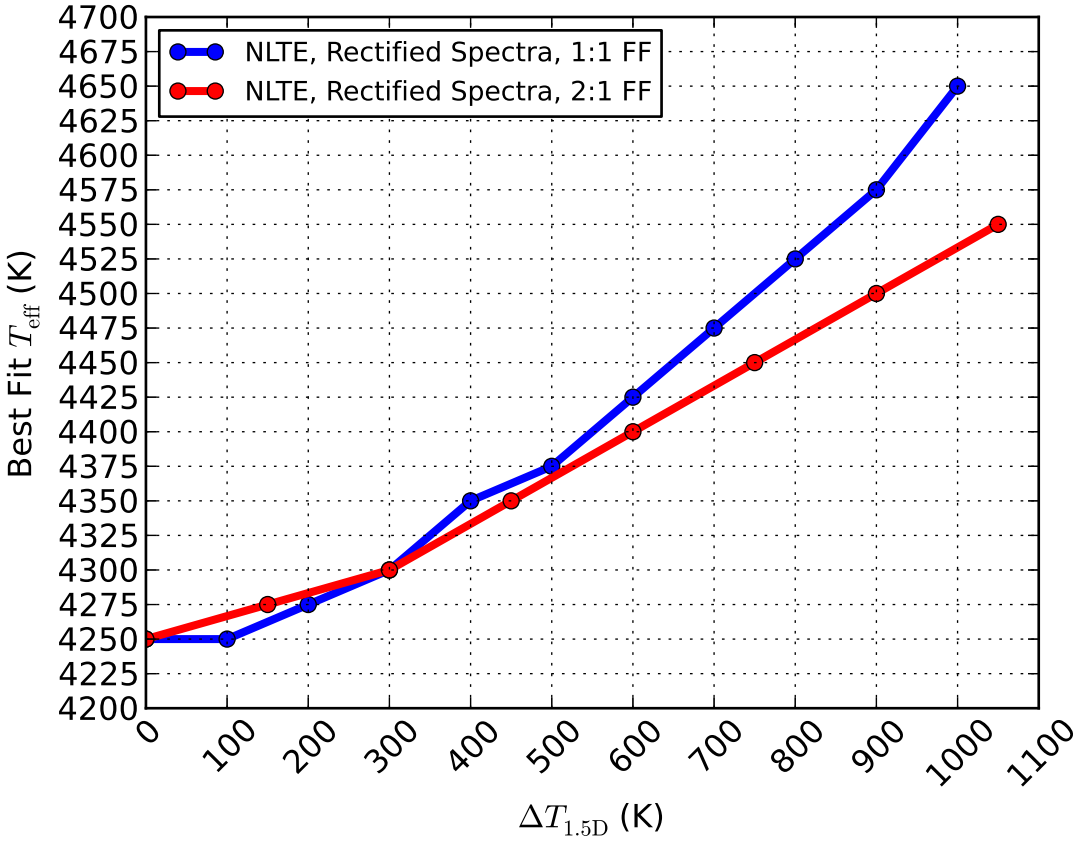

Figure 3.11: Same as Fig. 3.5, but for the rectified spectra.

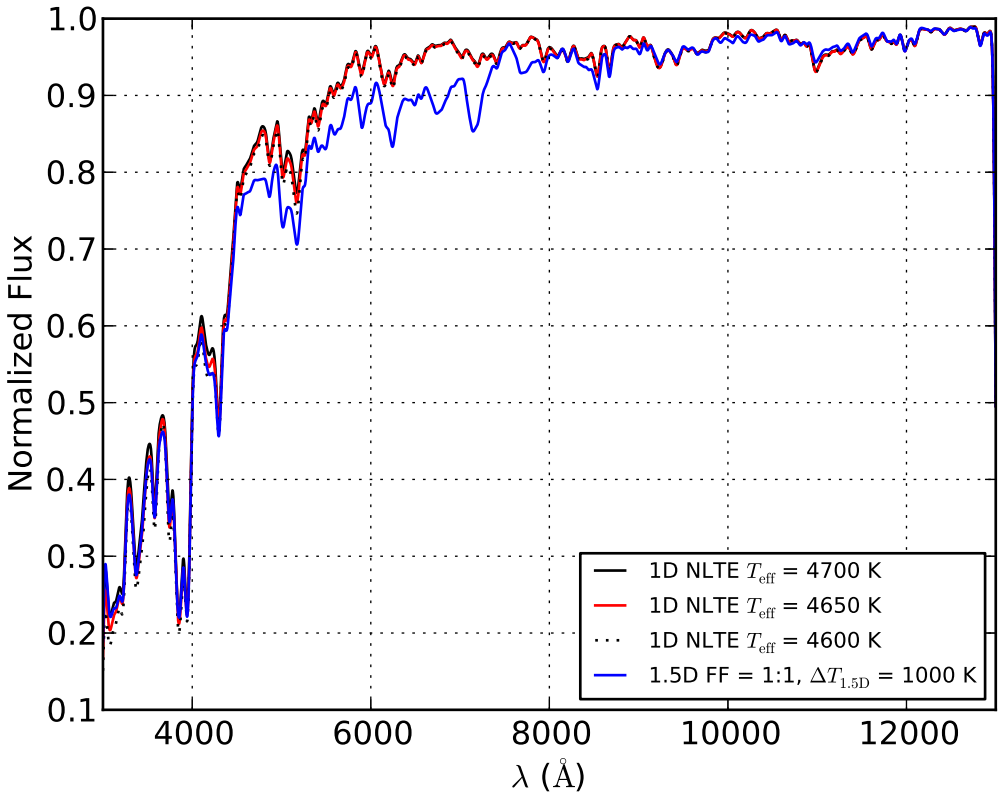

Figure 3.12: Same as Fig. 3.6 but for rectified spectra over the entire λ range.

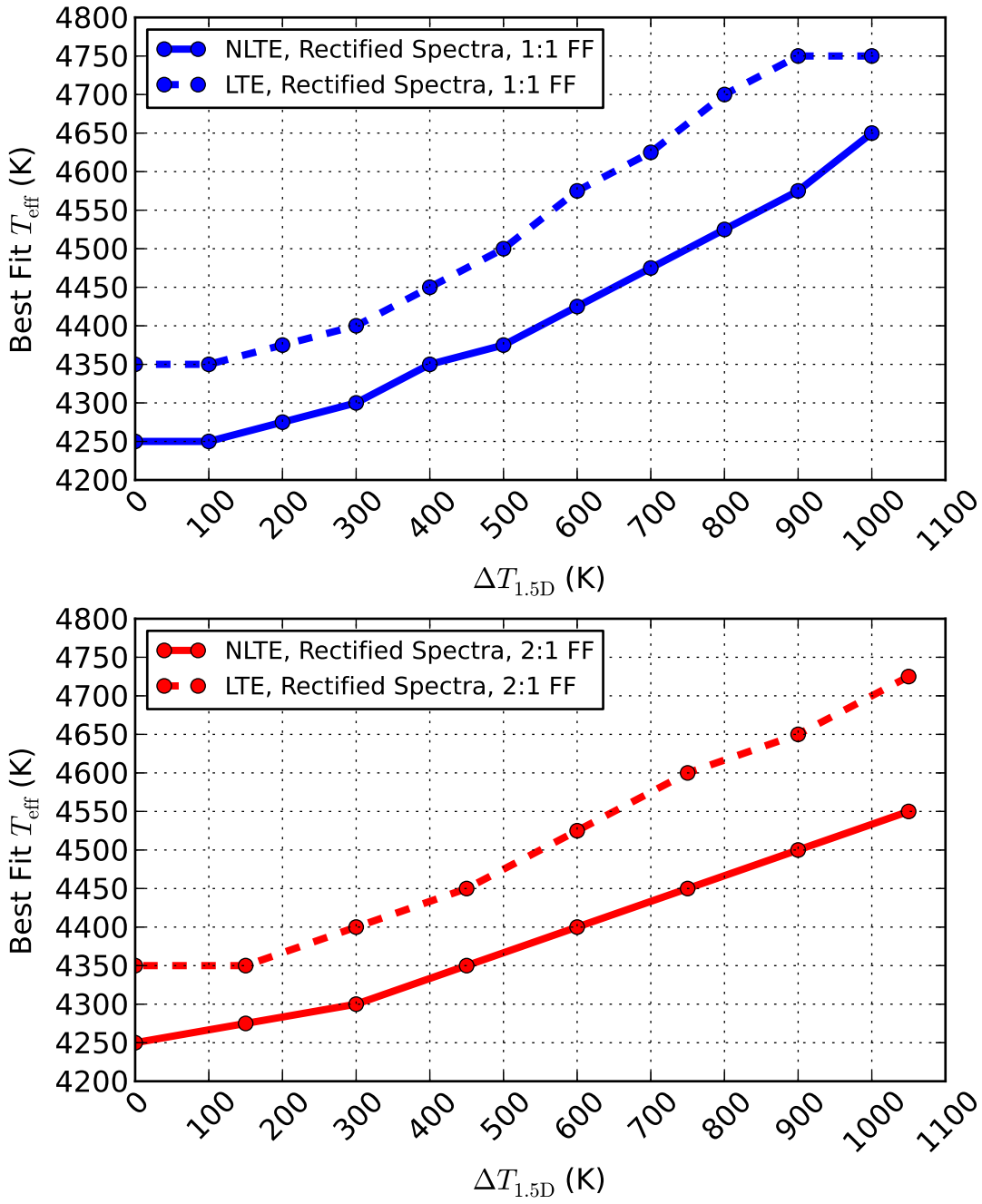

Figure 3.13: Same as Fig. 3.7, but for the rectified spectra. The data points for the LTE 1:1 FF fits at $\Delta T_{\rm 1.5D} = 900$ K and 1000 K are at the upper limit of the 1D grid of models and may not accurately represent what the best fitting $T_{\rm eff}$ values may be.

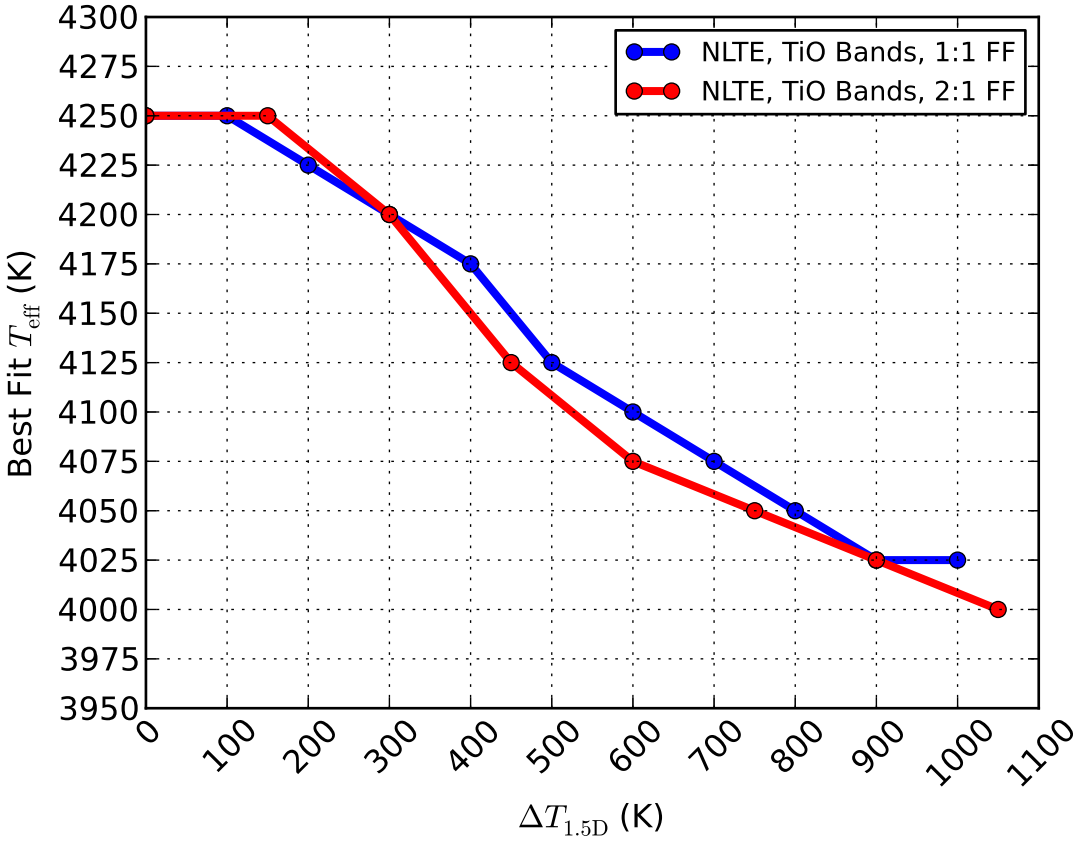

Figure 3.14: Same as Fig. 3.5, but from fitting TiO bands.

in strength so rapidly with decreasing $T_{\rm eff}$ that the hot component does not dominate the fit to the TiO band region as it does for the overall rectified spectra. The cool component now dominates the shape, with the hot component only mitigating the effect, pulling the fits to lower temperatures with increasing $\Delta T_{\rm 1.5D}$.

Fig. 3.15 is the same as Fig. 3.12, but shows the best fit and bracketing 1D spectra from fitting the TiO bands instead of the full λ range. The best fitting 1D NLTE rectified spectrum is a good match to the 1.5D spectrum at $\lambda \geq 5500$ Å, but is a very poor match between $\lambda = 5000$ Å and 5500 Å, where the overlapping TiO and MgH molecular features are poorly fit.

The LTE results are hotter than the respective NLTE results at each $\Delta T_{\rm 1.5D}$ for both choices of FF. This is not caused by Fe I overionization as in the previous four methods, instead it is an indirect effect of the difference of LTE and NLTE $T_{\rm Kin}\,(\tau)$ structures in the upper atmosphere. For a given $T_{\rm eff}$, NLTE models are generally hotter than LTE models in the upper atmosphere above $\tau_{12000} = 1$, as seen in Fig. 3.16. Because of this, more TiO molecules will collisionally dissociate in the upper atmosphere of a NLTE star than an LTE star, and NLTE stars will form weaker absorption features. Therefore, NLTE best fits will be required to have lower $T_{\rm eff}$ values to match the strength of the TiO absorption features. In this case $\Delta T_{\rm NLTE}$ is non constant as a function of $\Delta T_{\rm 1.5D}$, increasing from 50 K at $\Delta T_{\rm 1.5D} = 0$ K, to a local maximum of 100 K, then decreasing back to 75 K at maximum $\Delta T_{\rm 1.5D}$, for both FF. Fig. 3.17 shows this maximum $\Delta T_{\rm NLTE}$ occurring between $\Delta T_{\rm 1.5D} = 400$ K and 700 K.

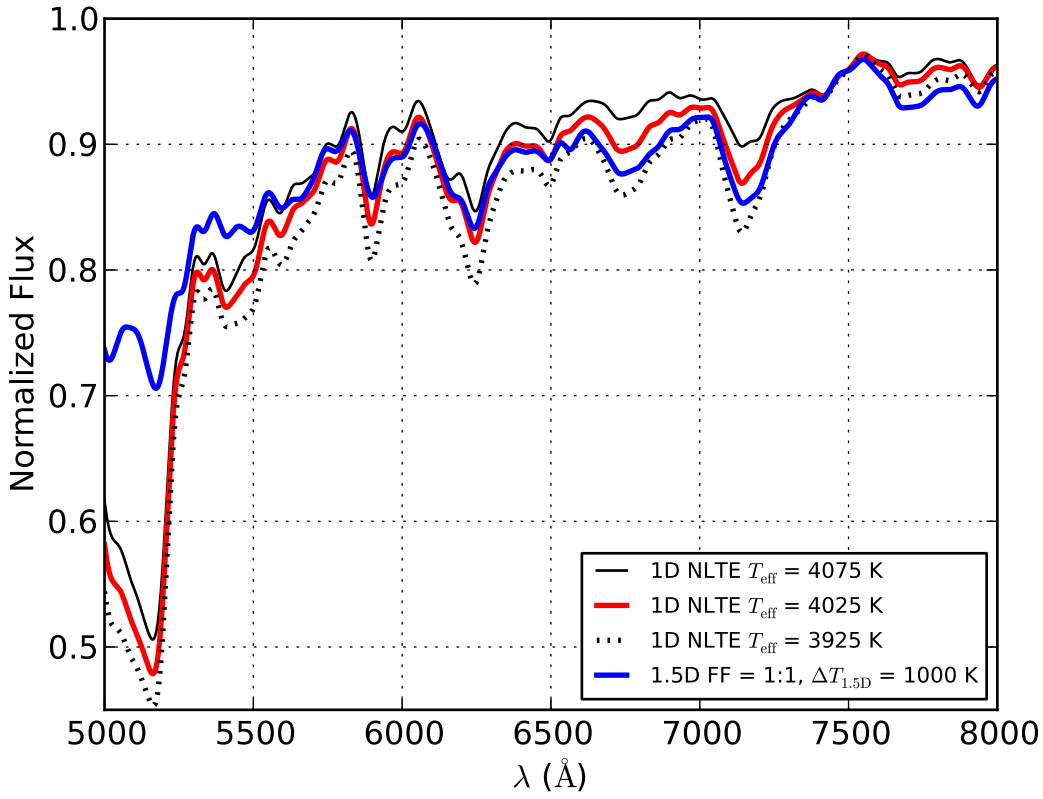

Figure 3.15: Same as Fig. 3.6 but for rectified spectra restricted to the TiO bands.

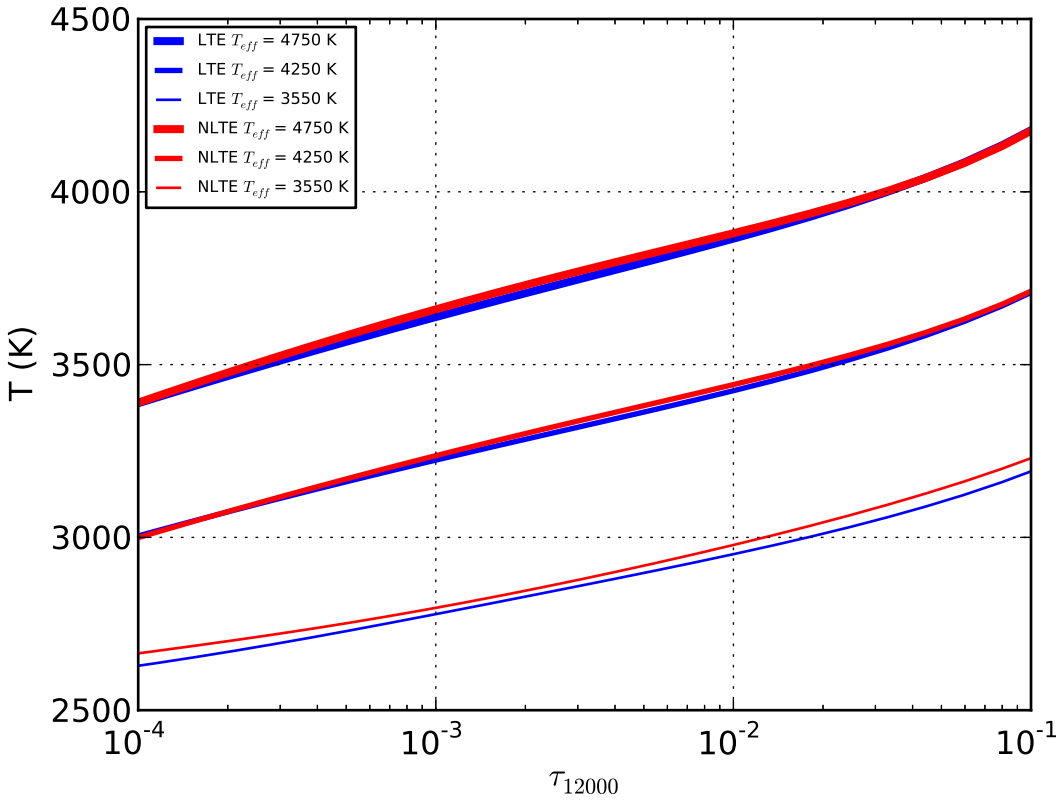

Figure 3.16: Enlarged section of Fig. 2.2. NLTE $T_{\rm Kin}$ (τ_{12000}) relations are seen to be hotter than LTE for a given $T_{\rm eff}$.

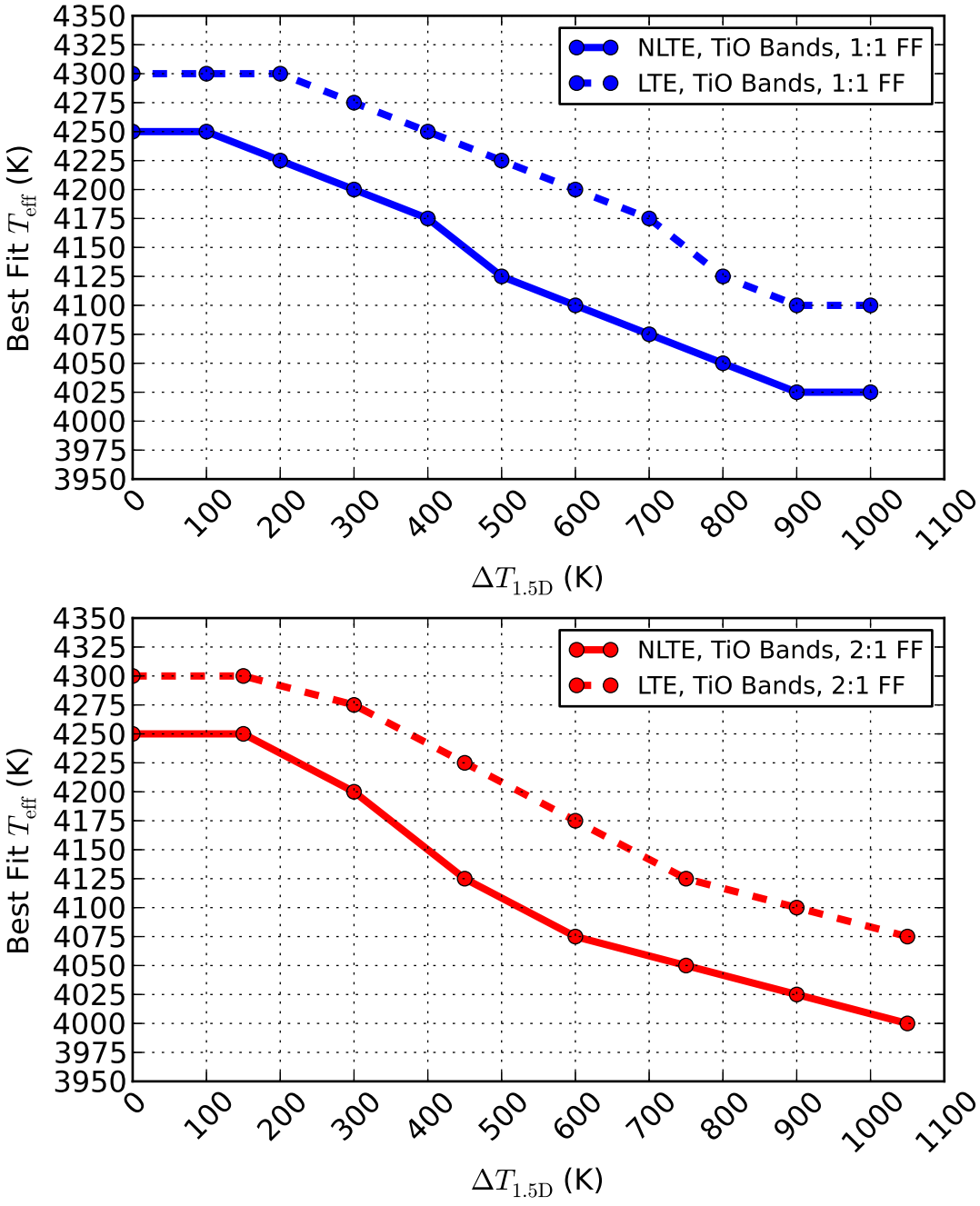

Figure 3.17: Same as Fig. 3.7, but from fitting TiO bands.

Table 3.1: Master Results Table for FF 1:1

NLTE

$\Delta T_{1.5\rm D}$	U_x-B_x	B-V	V-R	V-I	R-I	Absolute SED	Pinned SED	Rectified Spectra	TiO Bands
1000	4675	4650	4575	4425	4300	4450	4550	4650	4025
900	4625	4575	4500	4400	4275	4425	4500	4575	4025
800	4550	4525	4450	4375	4275	4400	4450	4525	4050
700	4500	4450	4400	4350	4275	4375	4425	4475	4075
600	4450	4400	4375	4325	4275	4350	4375	4425	4100
500	4375	4350	4325	4300	4275	4325	4350	4375	4125
400	4350	4325	4300	4275	4250	4300	4325	4350	4175
300	4300	4300	4275	4275	4250	4275	4300	4300	4200
200	4275	4275	4275	4250	4250	4275	4275	4275	4225
100	4250	4250	4250	4250	4250	4250	4250	4250	4250
0	4250	4250	4250	4250	4250	4250	4250	4250	4250

LTE

$\Delta T_{1.5\rm D}$	U_x-B_x	B-V	V-R	V-I	R-I	Absolute SED	Pinned SED	Rectified Spectra	TiO Bands
1000	4750	4725	4600	4475	4325	4500	4600	4750	4100
900	4750	4650	4525	4425	4325	4475	4575	4750	4100
800	4725	4575	4475	4400	4300	4450	4525	4700	4125
700	4675	4525	4425	4375	4300	4400	4475	4625	4175
600	4600	4475	4400	4350	4300	4375	4450	4575	4200
500	4550	4425	4350	4325	4300	4350	4400	4500	4225
400	4500	4375	4325	4300	4300	4325	4375	4450	4250
300	4450	4350	4300	4300	4300	4325	4350	4400	4275
200	4425	4325	4275	4300	4300	4300	4325	4375	4300
100	4400	4300	4275	4275	4300	4300	4300	4350	4300
0	4400	4300	4275	4275	4275	4300	4300	4350	4300

Table 3.2: Master Results Table for FF 2:1

NLTE

$\Delta T_{1.5\rm D}$	U_x-B_x	B-V	V-R	V-I	R-I	Absolute SED	Pinned SED	Rectified Spectra	TiO Bands
1050	4575	4575	4550	4425	4300	4425	4475	4550	4000
900	4525	4525	4475	4375	4250	4400	4450	4500	4025
750	4475	4450	4425	4325	4250	4350	4400	4450	4050
600	4400	4375	4350	4300	4250	4325	4350	4400	4075
450	4350	4325	4300	4275	4250	4300	4325	4350	4125
300	4300	4275	4275	4275	4250	4275	4275	4300	4200
150	4250	4250	4250	4250	4250	4250	4250	4275	4250
0	4250	4250	4250	4250	4250	4250	4250	4250	4250

LTE

$\Delta T_{1.5\rm D}$	U_x-B_x	B-V	V-R	V-I	R-I	Absolute SED	Pinned SED	Rectified Spectra	TiO Bands
1050	4750	4650	4575	4450	4325	4475	4550	4725	4075
900	4700	4575	4500	4400	4300	4425	4500	4650	4100
750	4625	4500	4450	4375	4275	4400	4450	4600	4125
600	4550	4450	4375	4325	4275	4375	4425	4525	4175
450	4500	4375	4325	4300	4300	4350	4375	4450	4225
300	4450	4325	4300	4300	4300	4325	4325	4400	4275
150	4400	4300	4275	4275	4300	4300	4300	4350	4300
0	4400	4300	4275	4275	4275	4300	4300	4350	4300

Chapter 4

Comparison with Observed Spectra of Arcturus

Arcturus (α Boo, HR5430, HD124897) is an example of a red giant that is used as a standard star. It is a type K1.5-2 IIIe star, whose spectrum displays emission lines. While this is not uncommon in red giant stars, Arcturus is a particularly strong example of this phenomenon for select lines (Moos et al. 1974; Brown et al. 2008). It is a cool, intermediate mass red giant star with $T_{\rm eff} = 4286 \pm 30$ K, $M = 1.08 \pm 0.06\ M_{\odot}$ and $\log g = 1.66 \pm 0.05$ (Ramírez & Allende Prieto 2011). With a visual magnitude of -0.04, it is the fourth brightest star in the night sky, and the brightest red giant star, even at a distance of 11.3 pc from earth. Arcturus has an absolute visual magnitude of -0.30, making it a very bright star, with a luminosity in the visual band of $L_{\rm V} \approx 110\ L_{\odot}$. It is also a moderately metal poor star, with $[{\rm Fe/H}] =$ -0.52 $\pm$ 0.04, as derived from Fe I lines in its spectrum, which is consistent with it's kinematics identifying it as a local thick-disk star.

Because Arcturus has stellar parameters similar to the reference model, it was selected as a candidate to test for gross evidence of inhomogeneities. Observed spectral data sets for Arcturus were visually compared with LTE and NLTE 1D and 1.5D spectra. Two sets of observed data were investigated, the spectrophotometric data of the Burnashev catalogue (Burnashev 1985), consisting of four observations averaged together, and a high resolution spectroscopic atlas of Arcturus (Hinkle

et al. 2000).

The Burnashev catalogue presents spectra for a large sample of stars, including Arcturus. The catalogue contains their own measurements made at the Crimean Astrophysical Observatory, measurements from the "Sternberg spectrophotometric catalogue" (Glushneva et al. 1984) consisting of data taken from 1970 to 1984 with the 40 cm and 60 cm telescopes of the Crimean Station of the Sternberg Astronomical Institute and the 50 cm telescope of the Fessenkov Astrophysical Institute, and measurements of Kharitonov et al. (1978) taken with the 50 cm Cassegrain telescope and spectrum scanner with a photomultiplier tube at the Fessenkov Astrophysical Institute from 1968 to 1986. These data sets all generally cover the λ range between 3200 Å and 8000 Å with $\Delta\lambda = 25$ Å or 50 Å, and have been re-reduced to a common spectrophotometric system by Burnashev. All three of these sources report data for Arcturus.

The Hinkle data set contains CCD observations of Arcturus with $R \sim 150000$ spanning the visible and near-IR regions between $\lambda = 3727$ Å and 9300 Å. The observations were made with the Coude Feed telescope on Kitt Peak with the spectrograph in the Echelle mode. The signal to noise ratio of the spectrum is reported to be ~ 1000 and the spectrum has been corrected for telluric absorption lines.

To allow for easy visual comparison, the Hinkle data were convolved with the same FWHM = 50 Å Gaussian kernel that the synthetic spectra were, and the Burnashev data were scaled from the observed flux at earth to stellar surface flux values and rectified using a PHOENIX synthetic continuum. To scale the Burnashev data, values of 21.06 $\pm$ 0.17 mas and 25.4 $\pm$ 0.2 $R_{\odot}$ were adopted for the angular diameter and stellar radius, respectively (Ramírez & Allende Prieto 2011). The synthetic continuum used in rectification was the one produced for rectifying the grid models with $T_{\rm eff} = 4300$ K, and the same rectification technique was used. Because the observed data sets spanned different λ ranges that did not fully overlap, the visual inspection was limited to the TiO band region between $\lambda = 4900$ Å and 7500 Å.

Fig. 4.1 shows the observed spectra over-plotted with the 1D NLTE and LTE synthetic spectra with $T_{\rm eff} = 4250$ K, and the two 1.5D spectra closest to the shape of the observed spectra across

this range, both with $\Delta T_{1.5\mathrm{D}} = 500$ K and 600 K and of 1:1 FF. In general, for both choices of FF, 1.5D stars with lower values of $\Delta T_{1.5\mathrm{D}}$ match up with most of the range well but do a poor job of matching the strength of the overlapping molecular features between $\lambda \approx 5000$ Å and 5250 Å caused by TiO and MgH. Conversely, 1.5D stars with higher values of $\Delta T_{1.5\mathrm{D}}$ match the molecular features well, but match the rest of the range poorly. While no 1.5D stars were closer to the profiles of the observed spectra across the entire λ range than the 1D stars, the two 1.5D stars depicted in Fig. 4.1 are a large improvement over the 1D stars for the molecular features, while not being much worse for the rest of the range, making them better matches than the 1D stars globally if not better at every sampling point.

To contrast the quality of the 1:1 FF fits in Fig. 4.1, examples of 1.5D spectra providing poor matches to the observed spectra are also plotted; Fig. 4.2 depicts the observed data compared with the 1.5D spectra having the minimum and maximum $\Delta T_{1.5\mathrm{D}}$ values for 1:1 FF, Fig. 4.3 shows the same for 2:1 FF and also includes the 2:1 FF 1.5D star with $\Delta T_{1.5\mathrm{D}} = 600$ K. In both cases, the 1.5D stars with the minimum $\Delta T_{1.5\mathrm{D}}$ show negligible differences from the 1D NLTE star. The 1:1 FF star with $\Delta T_{1.5\mathrm{D}} = 1000$ K does a better job of matching the overlapping TiO and MgH features than either the $\Delta T_{1.5\mathrm{D}} = 500$ K or 600 K 1.5D stars do, but is a poorer match for the rest of the spectrum to the extent that it is a poorer match globally. The same is true for the 2:1 FF star with $\Delta T_{1.5\mathrm{D}} = 1050$ K, except that the molecular features are not matched as well as in the 1:1 FF case, and the rest of the spectrum is matched even more poorly. These observations suggest that the best matching 1.5D star to the observed data is one with a mid range $\Delta T_{1.5\mathrm{D}}$ value, confirming the selection of $\Delta T_{1.5\mathrm{D}} = 500$ K or 600 K. The 2:1 FF star with $\Delta T_{1.5\mathrm{D}} = 600$ K is a worse match to the observed spectra everywhere than its 1:1 FF counterpart, suggesting that for Arcturus, the actual FF is closer to 1:1 than 2:1.

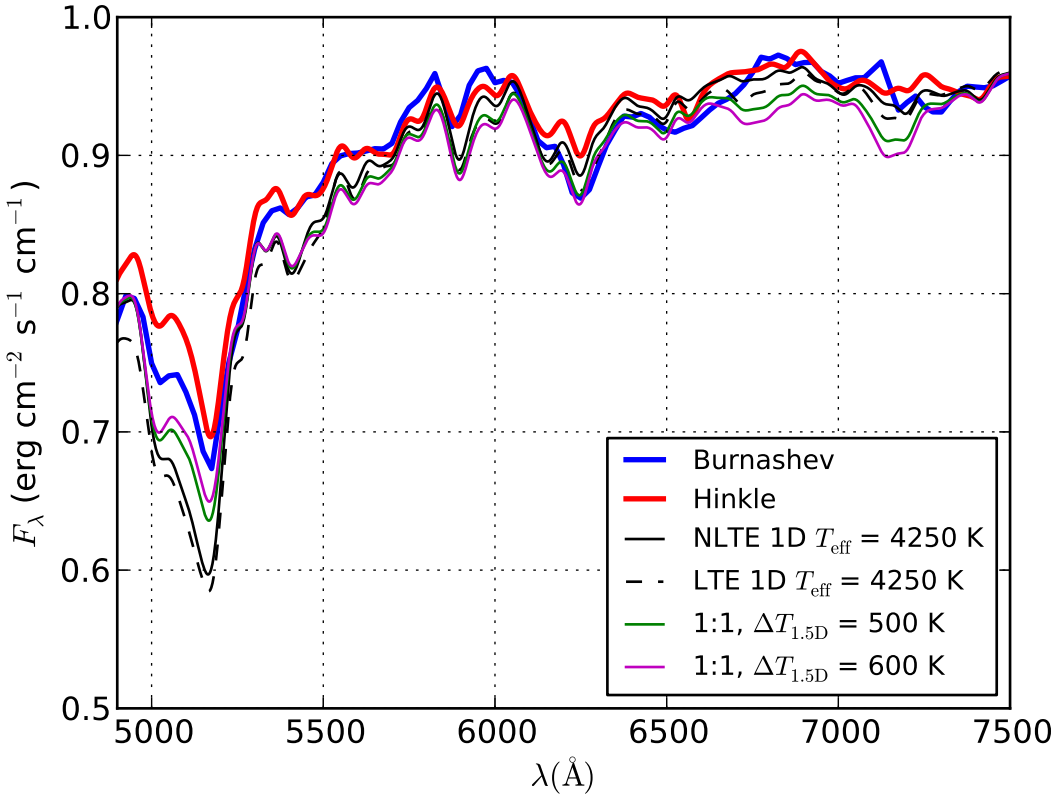

Figure 4.1: Observed Arcturus spectra of Hinkle et al. (2000) and of Burnashev (1985) compared to PHOENIX 1D LTE and NLTE spectra for $T_{\rm eff}$ =4250 K and best matching 1:1 FF 1.5D stars, having $\Delta T_{\rm 1.5D}$ =500 K and 600 K.

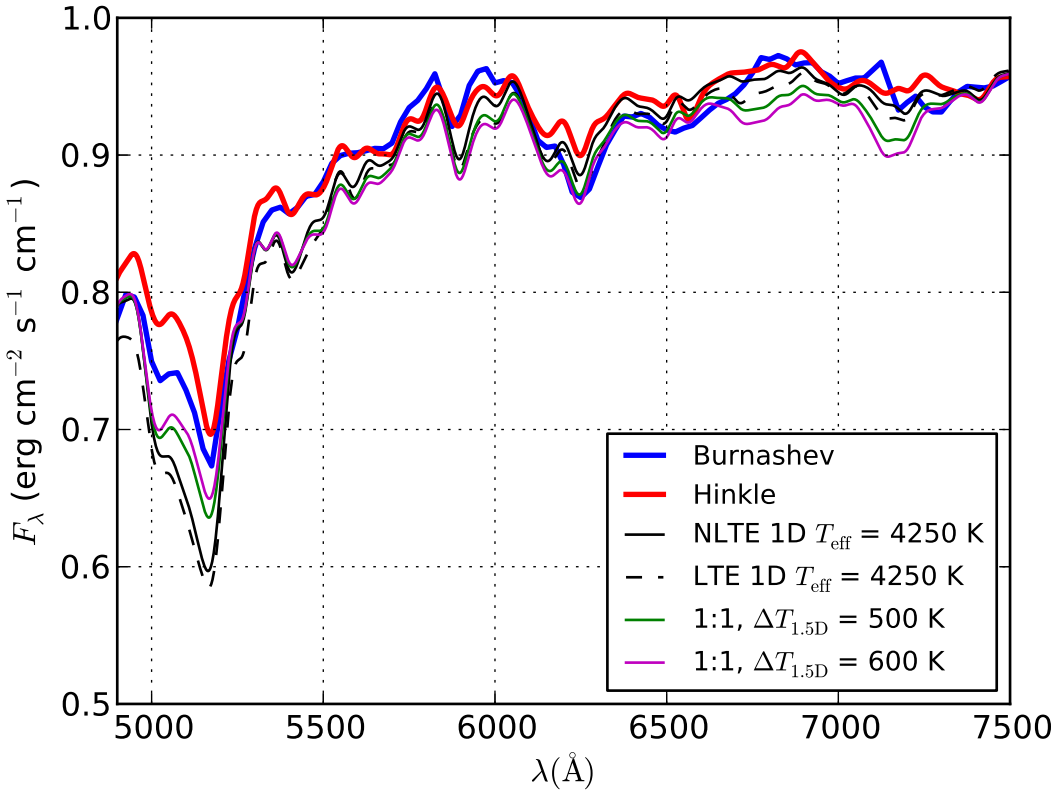

Figure 4.2: Same as Fig. 4.1, but with 1.5D stars having $\Delta T_{\rm 1.5D}$ =100 K and 1000 K.

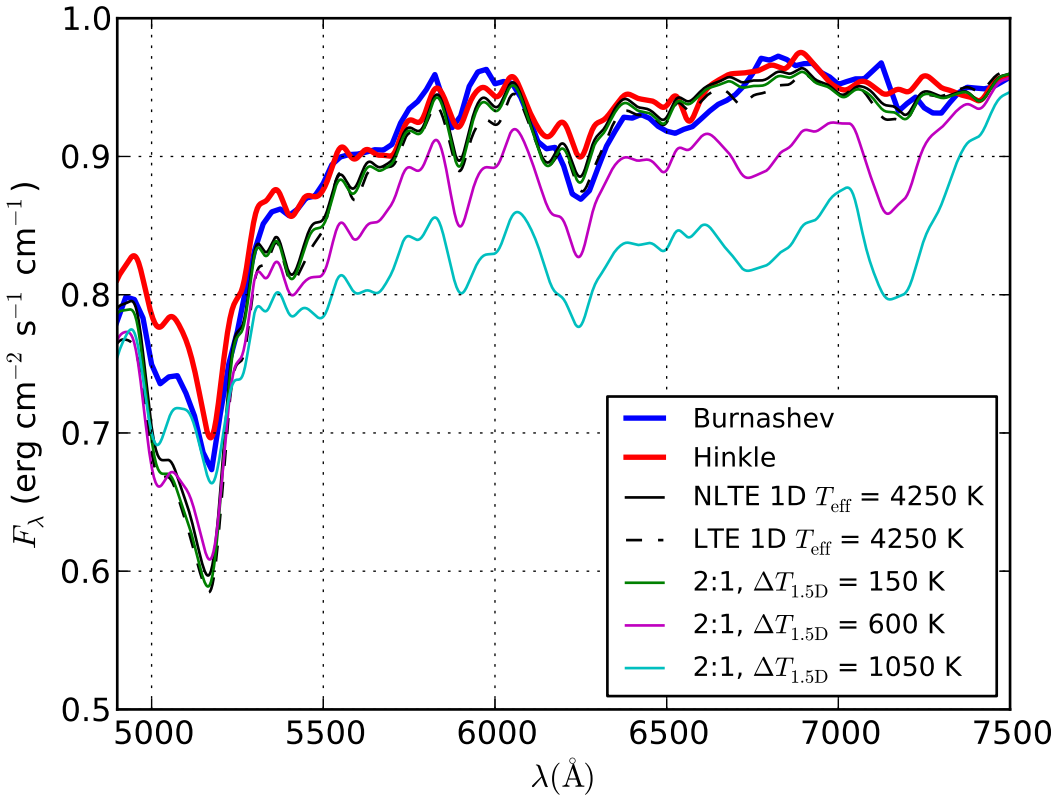

Figure 4.3: Same as Fig. 4.1 but with 2:1 FF 1.5D stars having $\Delta T_{\rm 1.5D}$ =150 K, 600 K, and 1050 K.

Chapter 5

Summary & Conclusions

The goal of this work has been to analyze the effects of the stellar atmospheric modelling assumptions of horizontal homogeneity and LTE on $T_{\rm eff}$ values inferred from SEDs and line profiles. The stellar atmosphere and spectrum synthesis code PHOENIX was used to generate a grid of spherical stellar atmosphere models in both LTE and NLTE, and to synthesize spectra for the models.

Spectra of target 2D "observed" stars were produced in the 1.5D approximation by linearly averaging two NLTE 1D spectra together under two different weighting schemes (FF), such that the $RJ\,T_{\rm eff}$ was 4250 K and the temperature difference between the 1D was as large as $\Delta T_{\rm 1.5D} = 1050$ K. The grid of LTE and NLTE 1D SEDs and spectra were fit to the observations to infer $T_{\rm eff}$ values for the 1.5D stars using five different approaches.

Spectrophotometric Methods

Photometric colours of 1D stars computed from synthetic UBVRI photometry were compared to 1.5D colours to assess the errors in photometrically derived $T_{\rm eff}$ values. For the five colour indices and both values of FF, the inferred value of $T_{\rm eff}$ was seen to increase with $\Delta T_{\rm 1.5D}$, and increased at a greater rate for indices that involved bluer wavebands. When the LTE and NLTE results were compared, the $T_{\rm eff}$ values inferred from fitting LTE colours were systematically higher than their NLTE counterparts. The magnitude of $\Delta T_{\rm NLTE}$ was approximately constant as a function of $\Delta T_{\rm 1.5D}$

in all cases. The value was largest when comparing U_x-B_x inferred $T_{\rm eff}$ values, at $\Delta T_{\rm NLTE} = 150$ K, and decreased for redder indices.

Absolute surface flux 1D SEDs were fit to the 1.5D SEDs to assess how changes to the predicted bolometric flux introduced by the modelling assumptions affect the inferred value of $T_{\rm eff}$. For both values of FF, the inferred value of $T_{\rm eff}$ was seen to increase with $\Delta T_{\rm 1.5D}$. This approach showed the lowest overall error of any of the full λ distribution fitting approaches in the inferred value of $T_{\rm eff}$; only 200 K at maximum $\Delta T_{\rm 1.5D}$. Again, the inferred $T_{\rm eff}$ values from fitting LTE SEDs were systematically higher than those from fitting NLTE SEDs, and the magnitude of $\Delta T_{\rm NLTE}$ was approximately constant as a function of $\Delta T_{\rm 1.5D}$.

Relative 1D SEDs normalized to the average flux in a 10 Å window in the R-J tail were fit to the 1.5D SEDs to assess how the modelling assumptions affect overall shape of the SED and the temperature sensitive spectral features located in the blue and near-UV bands. For both values of FF, the inferred value of $T_{\rm eff}$ was seen to increase with $\Delta T_{\rm 1.5D}$. The inferred $T_{\rm eff}$ values from fitting LTE SEDs were systematically higher than those from fitting NLTE SEDs, and the magnitude of $\Delta T_{\rm NLTE}$ was approximately constant as a function of $\Delta T_{\rm 1.5D}$.

Of the three spectrophotometric methods, the photometric colours give both the highest and the lowest errors on the estimates of $T_{\rm eff}$. At maximum $\Delta T_{\rm 1.5D}$, the U_x-B_x index fitting returned up to 425 K higher than the average $T_{\rm eff}$ for NLTE 1D stars and up to 500 K higher for LTE 1D stars, while the R-I index returned between 50 K and 75 K higher for NLTE and LTE, respectively. The absolute surface flux SED fitting resulted in error values similar to that of the V-I index at up to 200 K and 250 K higher than the average $T_{\rm eff}$ for NLTE and LTE, respectively. The relative SED fitting returned error values similar to the V-R index at up to 300 K and 350 K higher for NLTE and LTE, respectively.

Spectroscopic Methods

Rectified 1D spectra spanning a wavelength distribution between $\lambda = 3000$ Å and 13000 Å were fit to the 1.5D spectra to assess how the modelling assumptions change the predicted strength

of spectral features. For both values of FF, the inferred value of $T_{\rm eff}$ was seen to increase with $\Delta T_{\rm 1.5D}$. It is important to note that this result is consistent with the spectrophotometric results, even though it is arrived at through a complimentary method. This approach showed the highest overall error of any of the full spectrum fitting approaches in the inferred value of $T_{\rm eff}$; 400 K at maximum $\Delta T_{\rm 1.5D}$. The inferred $T_{\rm eff}$ values from fitting LTE spectra were systematically higher than those from fitting NLTE spectra, and the magnitude of $\Delta T_{\rm NLTE}$ was approximately constant as a function of $\Delta T_{\rm 1.5D}$.

Predicted line profiles for the important 1D TiO bands spanning a wavelength range between $\lambda = 5500$ Å and 8000 Å were fit to the 1.5D TiO bands to assess how the strength of molecular features found primarily in the cold component of the 1.5D stars affect the inferred value of $T_{\rm eff}$. This was the only approach to show the inferred value of $T_{\rm eff}$ decreasing with increasing $\Delta T_{\rm 1.5D}$. The rapid nonlinear growth of molecular features with decreasing temperature became the dominant aspect in determining the $T_{\rm eff}$ value, over the nonlinear contribution to the average flux from the higher temperature 1.5D component. The inferred $T_{\rm eff}$ values from fitting LTE spectra were still systematically higher than those from fitting NLTE spectra, and the magnitude of $\Delta T_{\rm NLTE}$ was approximately constant as a function of $\Delta T_{\rm 1.5D}$.

In this work we have shown that the approximations of both horizontal homogeneity and LTE introduce errors in the value of $T_{\rm eff}$ inferred from fitting quantities derived from models to observed quantities. By assuming both horizontal homogeneity and LTE, the inferred $T_{\rm eff}$ values may differ from the average $T_{\rm eff}$ of a star by 500 K or more, depending on the quantity used to infer the $T_{\rm eff}$. Of the two values of FF, 1:1 produced hotter values of inferred $T_{\rm eff}$ in general. In simulating horizontal inhomogeneities it was seen that the bolometric flux of a 1.5D star increased with $\Delta T_{\rm 1.5D}$, and a percentage of the flux was redistributed at bluer wavelengths. Spectral line features in general appeared to have been produced by a star hotter than the average $T_{\rm eff}$, except that molecular features found in cooler stars were also present in the spectra. Furthermore, for all five approaches, there

appeared to be no correlation between the errors in inferred $T_{\rm eff}$ values from assuming horizontal homogeneity and those from assuming LTE, and any deviation of $\Delta T_{\rm NLTE}$ from a constant value is assumed to be caused by the temperature resolution of the grid of 1D spectra.

Finally, when comparing 1.5D spectra to spectroscopic and rectified spectrophotometric observations of Arcturus, neither 1D or 1.5D spectra are a perfect match across all wavebands. The 1D spectra fail to correctly predict the strength of molecular features, and the 1.5D ones overpredict the strength of weaker absorption features. The 1.5D stars with 1:1 FF and $\Delta T_{\rm 1.5D}$ values of 500 K and 600 K are globally the closest matching spectra to the observations, being slightly worse matches to the weaker features than 1D spectra, but greatly improving the predicted strength of molecular features. If Arcturus does host horizontal inhomogeneities of the type simulated in this work, it is possible they are of 1:1 FF rather than 2:1, and that they are of moderate strength with $\Delta T_{\rm 1.5D} \approx 550$ K.

Bibliography

Alves-Brito, A., Meléndez, J., Asplund, M., Ramírez, I., & Yong, D. (2010). Chemical similarities between Galactic bulge and local thick disk red giants: O, Na, Mg, Al, Si, Ca, and Ti. A&A, 513, A35.

Asplund, M., Grevesse, N., Sauval, A. J., & Scott, P. (2009). The Chemical Composition of the Sun. ARA&A, 47, 481–522.

Baron, E. & Hauschildt, P. H. (1998). Parallel Implementation of the PHOENIX Generalized Stellar Atmosphere Program. II. Wavelength Parallelization. ApJ, 495, 370.

Bergemann, M., Kudritzki, R. P., Davies, B., Plez, B., Gazak, Z., & Chiavassa, A. (2013). <3D> NLTE line formation in the atmospheres of red supergiants. In *EAS Publications Series*, volume 60 of *EAS Publications Series* (pp. 103–109).

Bessell, M. S. (1990). UBVRI passbands. PASP, 102, 1181–1199.

Brott, I. & Hauschildt, P. H. (2005). A PHOENIX Model Atmosphere Grid for Gaia. In C. Turon, K. S. O'Flaherty, & M. A. C. Perryman (Eds.), *The Three-Dimensional Universe with Gaia*, volume 576 of *ESA Special Publication* (pp. 565).

Brown, K. I. T., Gray, D. F., & Baliunas, S. L. (2008). Long-Term Spectroscopic Monitoring of Arcturus. ApJ, 679, 1531–1540.

Burnashev, V. I. (1985). Catalogue of data on energy distribution in spectra of stars in a uniform spectrophotometric system. *Abastumanskaia Astrofizicheskaia Observatoriia Byulleten*, 59, 83–90.

Caffau, E., Ludwig, H.-G., Steffen, M., Freytag, B., & Bonifacio, P. (2011). Solar Chemical Abundances Determined with a CO5BOLD 3D Model Atmosphere. Sol. Phys., 268, 255–269.

Carretta, E., Bragaglia, A., Gratton, R. G., Recio-Blanco, A., Lucatello, S., D'Orazi, V., & Cassisi, S. (2010). Properties of stellar generations in globular clusters and relations with global parameters. A&A, 516, A55.

Carretta, E. & Gratton, R. G. (1997). Abundances for globular cluster giants. I. Homogeneous metallicities for 24 clusters. A&AS, 121, 95–112.

Chiavassa, A., Collet, R., Casagrande, L., & Asplund, M. (2010). Three-dimensional hydrodynamical simulations of red giant stars: semi-global models for interpreting interferometric observations. A&A, 524, A93.

Collet, R., Asplund, M., & Trampedach, R. (2007). Three-dimensional hydrodynamical simulations of surface convection in red giant stars. Impact on spectral line formation and abundance analysis. A&A, 469, 687–706.

Collet, R., Asplund, M., & Trampedach, R. (2008). Beyond 1D: spectral line formation with 3D hydrodynamical model atmospheres of red giants. Mem. Soc. Astron. Italiana, 79, 649.

Collet, R., Nordlund, Å., Asplund, M., Hayek, W., & Trampedach, R. (2009). Abundance analysis of the halo giant HD 122563 with three-dimensional model stellar atmospheres. Mem. Soc. Astron. Italiana, 80, 719.

Cox, A. N. (2000). *Allen's astrophysical quantities*.

Cunha, K. & Smith, V. V. (2006). Chemical Evolution of the Galactic Bulge as Derived from High-Resolution Infrared Spectroscopy of K and M Red Giants. ApJ, 651, 491–501.

Davies, B., Kudritzki, R.-P., Plez, B., Trager, S., Lançon, A., Gazak, Z., Bergemann, M., Evans, C., & Chiavassa, A. (2013). The Temperatures of Red Supergiants. ApJ, 767, 3.

Glushneva, I. N., Doroshenko, I. B., Voloshina, V. T., Mossakovskaya, L. V., Ovchinnikov, S. K., & Khruzina, T. S. (1984). Energy Distribution Data in the Spectra of 72 Stars in the Region Lambda 3200A to 7600A. *Trudy Gosudarstvennogo Astronomicheskogo Instituta*, 54, 3.

Hauschildt, P. H., Baron, E., & Allard, F. (1997). Parallel Implementation of the PHOENIX Generalized Stellar Atmosphere Program. ApJ, 483, 390.

Hayek, W., Asplund, M., Collet, R., & Nordlund, Å. (2011). 3D LTE spectral line formation with scattering in red giant stars. A&A, 529, A158.

Hinkle, K., Wallace, L., Valenti, J., & Harmer, D. (2000). *Visible and Near Infrared Atlas of the Arcturus Spectrum 3727-9300 A*.

Hoffleit, D. & Jaschek, C. . (1991). *The Bright star catalogue*.

Kharitonov, A. V., Tereshchenko, V. M., & Kniazeva, L. N. (1978). *Svodnyi spektrofotometricheskii katalog zvezd.*

Kučinskas, A., Ludwig, H.-G., Steffen, M., Dobrovolskas, V., Klevas, J., Prakapavičius, D., Caffau, E., & Bonifacio, P. (2013a). The influence of convection on the atmospheric structures and observable properties of red giant stars. *Memorie della Societa Astronomica Italiana Supplementi*, 24, 68.

Kučinskas, A., Steffen, M., Ludwig, H.-G., Dobrovolskas, V., Ivanauskas, A., Klevas, J., Prakapavičius, D., Caffau, E., & Bonifacio, P. (2013b). Three-dimensional hydrodynamical CO^{5}BOLD model atmospheres of red giant stars. II. Spectral line formation in the atmosphere of a giant located near the RGB tip. A&A, 549, A14.

Lee, M. G., Freedman, W. L., & Madore, B. F. (1993). The Tip of the Red Giant Branch as a Distance Indicator for Resolved Galaxies. ApJ, 417, 553.

Ludwig, H.-G. & Kučinskas, A. (2012). Three-dimensional hydrodynamical CO^{5}BOLD model atmospheres of red giant stars. I. Atmospheric structure of a giant located near the RGB tip. A&A, 547, A118.

Magic, Z., Collet, R., Asplund, M., Trampedach, R., Hayek, W., Chiavassa, A., Stein, R. F., & Nordlund, Å. (2013a). The Stagger-grid: A Grid of 3D Stellar Atmosphere Models - I. Methods and General Properties. *ArXiv e-prints*.

Magic, Z., Collet, R., Hayek, W., & Asplund, M. (2013b). The Stagger-grid: A Grid of 3D Stellar Atmosphere Models - II. Horizontal and Temporal Averaging and Spectral Line Formation. *ArXiv e-prints*.

Makarov, D., Makarova, L., Rizzi, L., Tully, R. B., Dolphin, A. E., Sakai, S., & Shaya, E. J. (2006). Tip of the Red Giant Branch Distances. I. Optimization of a Maximum Likelihood Algorithm. AJ, 132, 2729–2742.

Martins, F., Schaerer, D., & Hillier, D. J. (2005). A new calibration of stellar parameters of Galactic O stars. A&A, 436, 1049–1065.

Mashonkina, L., Ludwig, H.-G., Korn, A., Sitnova, T., & Caffau, E. (2013). Signs of atmospheric inhomogeneities in cool stars from 1D-NLTE analysis of iron lines . *Memorie della Societa Astronomica Italiana Supplementi*, 24, 120.

Mathur, S., Hekker, S., Trampedach, R., Ballot, J., Kallinger, T., Buzasi, D., García, R. A., Huber, D., Jiménez, A., Mosser, B., Bedding, T. R., Elsworth, Y., Régulo, C., Stello, D., Chaplin, W. J., De Ridder, J., Hale, S. J., Kinemuchi, K., Kjeldsen, H., Mullally, F., & Thompson, S. E. (2011). Granulation in Red Giants: Observations by the Kepler Mission and Three-dimensional Convection Simulations. ApJ, 741, 119.

Meléndez, J., Asplund, M., Alves-Brito, A., Cunha, K., Barbuy, B., Bessell, M. S., Chiappini, C., Freeman, K. C., Ramírez, I., Smith, V. V., & Yong, D. (2008). Chemical similarities between Galactic bulge and local thick disk red giant stars. A&A, 484, L21–L25.

Moos, H. W., Linsky, J. L., Henry, R. C., & McClintock, W. (1974). High-Spectral Measurements of the H i λ1216 and MG II λ 2800 Emissions from Arcturus. ApJ, 188, L93.

Pilachowski, C. A., Sneden, C., & Wallerstein, G. (1983). The chemical composition of stars in globular clusters. ApJS, 52, 241–287.

Ramírez, I. & Allende Prieto, C. (2011). Fundamental Parameters and Chemical Composition of Arcturus. ApJ, 743, 135.

Ramírez, I. & Meléndez, J. (2005). The Effective Temperature Scale of FGK Stars. I. Determination of Temperatures and Angular Diameters with the Infrared Flux Method. ApJ, 626, 446–464.

Rizzi, L., Tully, R. B., Makarov, D., Makarova, L., Dolphin, A. E., Sakai, S., & Shaya, E. J. (2007). Tip of the Red Giant Branch Distances. II. Zero-Point Calibration. ApJ, 661, 815–829.

Ross, J. E. & Aller, L. H. (1976). The chemical composition of the sun. *Science*, 191, 1223–1229.

Salaris, M. & Cassisi, S. (1998). A new analysis of the red giant branch 'tip' distance scale and the value of the Hubble constant. MNRAS, 298, 166–178.

Sheminova, V. A. (2012). The Wings of Ca ii H and K as Photospheric Diagnostics and the Reliability of One-Dimensional Photosphere Modeling. Sol. Phys., 280, 83–102.

Short, C. I., Campbell, E. A., Pickup, H., & Hauschildt, P. H. (2012). Modeling the near-UV Band of GK Stars. II. Non-LTE Models. ApJ, 747, 143.

Short, C. I. & Hauschildt, P. H. (2003). Atmospheric Models of Red Giants with Massive-Scale Non-Local Thermodynamic Equilibrium. ApJ, 596, 501–508.

Short, C. I. & Hauschildt, P. H. (2005). A Non-LTE Line-Blanketed Model of a Solar-Type Star. ApJ, 618, 926–938.

Short, C. I. & Hauschildt, P. H. (2006). NLTE Strontium and Barium in Metal-poor Red Giant Stars. ApJ, 641, 494–503.

Short, C. I. & Hauschildt, P. H. (2009). Non-LTE Modeling of the Near-Ultraviolet Band of Late-Type Stars. ApJ, 691, 1634–1647.

Stanek, K. Z., Udalski, A., Szymanski, M., Kaluzny, J., Kubiak, M., Mateo, M., & Krzeminski, W. (1997). Modeling the Galactic Bar Using Red Clump Giants. ApJ, 477, 163.

Tremblay, P.-E., Ludwig, H.-G., Freytag, B., Steffen, M., & Caffau, E. (2013). Granulation properties of giants, dwarfs, and white dwarfs from the CIFIST 3D model atmosphere grid. *ArXiv e-prints*.

Uitenbroek, H. & Criscuoli, S. (2011). Why One-dimensional Models Fail in the Diagnosis of Average Spectra from Inhomogeneous Stellar Atmospheres. ApJ, 736, 69.